University of Alberta

Graphene-based Nanodevice Design and Modeling

by

Huaixiu Zheng ©

Huaixiu Zheng ©

A thesis submitted to the Faculty of Graduate Studies and Research
in partial fulfillment of the requirements for the degree of

Master of Science

Electrical and Computer Engineering

Edmonton, Alberta
Fall 2007

Your file Votre référence
ISBN: 978-0-494-33383-9
Our file Notre référence
ISBN: 978-0-494-33383-9

Abstract

As semiconducting devices are fast approaching their physical limitations, there are urgent needs to search for next generation nanodevices. Among various nanodevices including carbon nanotube devices, quantum devices and spintronic devices, graphene-based devices are most promising. Graphene is a flat monolayer of carbon atoms tightly packed into a two-dimensional (2D) honeycomb lattice. In this thesis, we present graphene-based device designs and modeling. The contributions include (i) Deriving the analytical solution of the wave function and energy dispersion of armchair graphene nanoribbons (GNRs) based on the tight-binding (TB) approximation. (ii) Discussing the effects of chemical edge modifications on the structural and electronic properties of GNRs with combined first-principles and TB calculations. Theoretical results show that addends can change the band structures of armchair GNRs and even result in an observable metal-to-insulator transition. (iii) Proposing the designs of three novel nanoelectronic devices using graphene nanoribbons according to the Landauer-Buttiker formula and the tight-binding model. By applying a gate voltage in the junction, a switch, a Z-shaped transmission gate and a field-effect transistor can be realized, respectively. Our device model provides a new platform for designing functional graphene-based molecular devices in future.

Acknowledgments

My graduate study at the Electrical and Computer Engineering Department, University of Alberta has been a rewarding experiment for me, both personally and scientifically. I would like to acknowledge those who have helped me and contributed my research during this fruitful period.

First of all, I would like to express my great appreciation to my supervisor, Prof. Jie Chen, for his constant encouragement and support. It was a nice thing to work for someone who is always available for help and care about research progress. In addition, I highly appreciated the space and freedom he gave me to try and investigate new ideas. I also thank Prof. Qinwei Shi at the University of Science and Technology of China for his guidance on the computation techniques and physical illustrations. I am also grateful to Professors Mani Vaidyanathan and Michael Woodside for serving on my defense committee.

My colleagues in Dr. Jie Chen's group were a great help during this period. Particularly, it is a privilege to team up with Zhengfei Wang, whose expertise in theoretical techniques was very crucial to my project. I benefited greatly from his sharing and the explanation of many physical concepts in an understandable way. I also enjoyed working with other colleagues, Huifei Rao, Jing Yang, Yao Yao, Jianliu Huang, Tao Kong, Jie Zeng, Woon Tiang Ang, Tao Xu, and Tingting Liu. Conservations and interactions with them made the lab a memorable experience in my life. Also, I thank

Thomas McIntyre, Nathanael Wu and Stephen Thornhill for their help in finalization of this thesis.

I also want to express my gratitude to friends and family who constantly encouraged and supported me. Especially, I am grateful to have met and been blessed by my close friend Huanyu Chen. I thank my family for their belief in me and their unconditional encouragement for my career and life.

Last but not least, I would like to acknowledge the funding support from NSREC Discovery program.

Contents

List of Figures

Chapter 1

Introduction

Graphene is a flat carbon sheet. Due to its unique quantum effects and electronic properties, researchers predict that graphene-based devices can replace silicon devices and revolutionize future nanoelectronic devices and circuits. [1 -3]

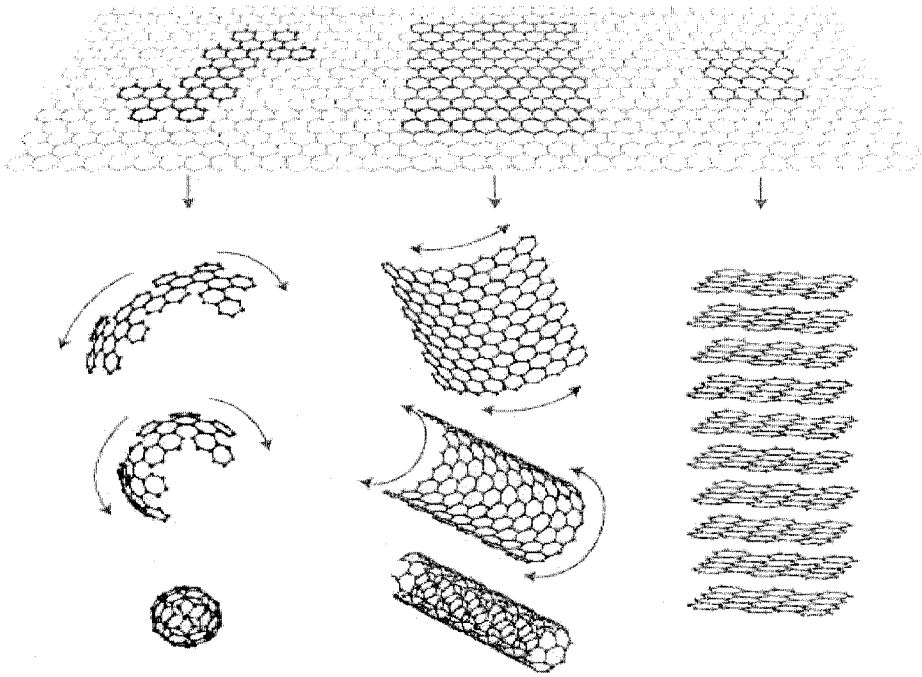

Fig. 1.1: *Various graphitic forms. Graphene is a 2D building material for carbon materials. It can be wrapped up into 0D buckyballs, or rolled into 1D nanotubes or stacked into 3D graphite. Reproduced with permission from A. K. Geim, and K. S. Novoselov, Nature Mater.* ***6****, 183 (2006).*

Carbon exists in various forms, such as 'buckyballs', diamonds, nanotubes and graphite, to name a few. Graphene is a flat monolayer of carbon atoms tightly packed into a two-dimensional (2D) honeycomb lattice, and is the basic building block of graphitic materials. It can be wrapped up into zero-dimensional (0D) fullerenes, rolled into one-dimensional (1D) nanotubes or stacked into three-dimensional (3D) graphite as shown in Fig.1.1. In the past, researchers had projected that planar graphene alone could not exist in the free state because it is not stable compared to other formations of curved structures, such as soot, fullerenes, and nanotubes [4-5].

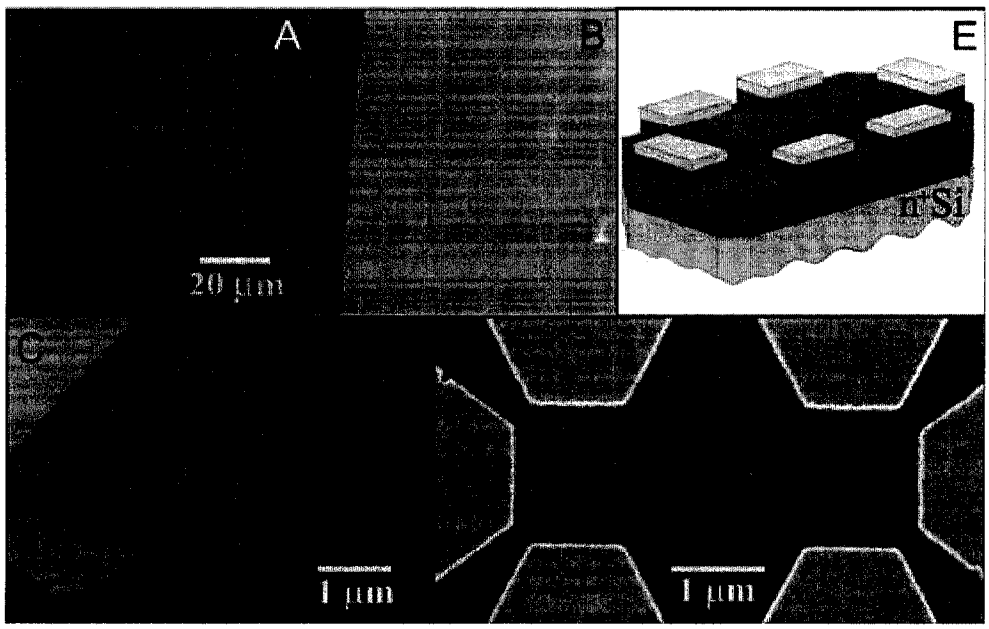

Fig. 1.2: *Single- and multiple-layer graphene made by Geim's group: (A) Photograph of multilayer graphene flake with thickness ~3nm on top of an oxidized Si wafer. (B) Atomic force microscope (AFM) image of a 2um by 2um area of above a flake of graphene. (C) AFM image of single-layer graphene. (D)*

*Scanning electron microscope image of the experimental devices prepared from few-layer graphene. (E) Schematic view of the device in (D). Reproduced with permission from K. S. Novoselov et al., Science **306**, 666 (2004).*

In 2004, André Geim at the University of Manchester, UK and his Russian colleagues successfully separated graphene from graphite. The resulting graphene is a one atom thick layer of carbon. [3] The graphene films were prepared by mechanical exfoliation (repeated peeling) of small mesas of highly oriented pyrolytic graphite. This approach is very reliable and allows us to prepare few-layer graphite (FLG) films up to 10um in size as shown in the Fig. 1.2. These FLG films can even be viewed by the naked eye. Electronic devices have been created with the obtained graphene films [3].

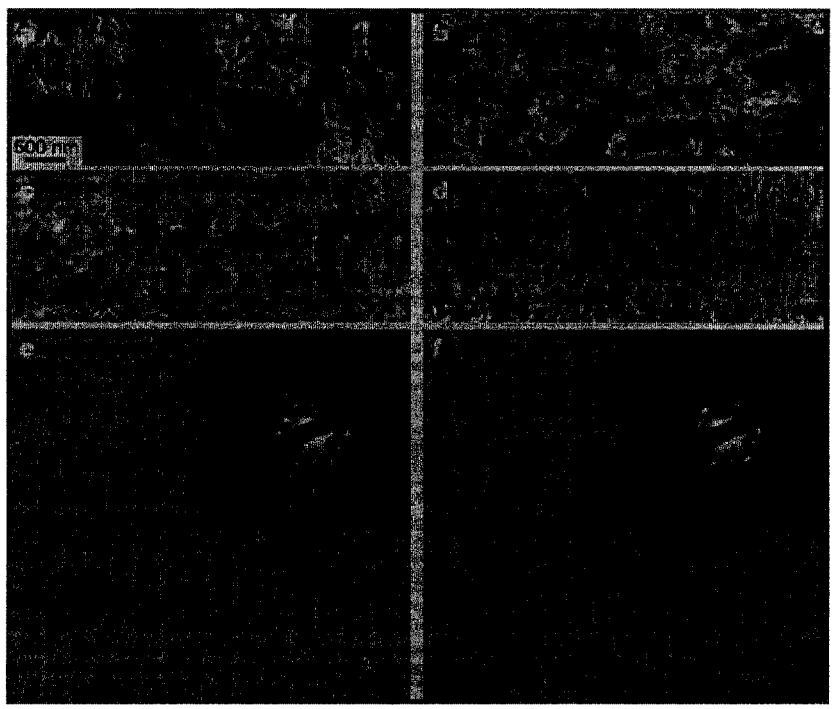

Fig. 1.3: *SEM and TEM images of a graphene-based composite [6]. **a-d**, SEM images of the microtomed composites of the graphene sheets at different concentrations (vol. %): **a**, 0.24; **b**, 0.96; **c**, 1.44; **d**, 2.4. e, f, High-resolution phase contrast images and SAED patterns (inset), which show the honeycomb patterned lattices.*

Later on, Rodney Ruoff and his team at Northwestern University came up with a chemical synthesizing method to make large amounts of graphene embedded in a polymer matrix [6] as shown in Fig. 1.3. The researchers started with graphite oxide —graphite with oxygen-containing chemical groups attached. After further chemical modifications and treatments with ultrasound, the graphite oxide was separated into layers, and dispersed through a solvent in which a polymer, such as polystyrene, was dissolved. Chemical reduction further removed most of the oxygen groups, and left behind graphene sheets crumpled within a solid polymer [6]. The resulting material is strong, and electrically and thermally conducting. Such properties are similar to those of carbon nanotube composites, which isn't surprising to us because a sheet of graphene is basically an unrolled nanotube. However, the resulting graphene-based composites produced by chemical method are cheaper and more reliable compared to the graphene obtained by mechanical method. As a result, this chemical process is perfect for making materials that are lightweight, yet strong and conducting, such as aircraft fuselages.

To-date, single- or few- layer graphene can be produced by either the

mechanical exfoliation method [3] or the chemical method [6]. The resulting graphene films are stable and have already shown interesting physical properties and great potential in various applications.

1.1 Graphene – An Interesting Material

Graphene, a two-dimensional material, shows exceptionally high crystal structure and electronic properties. It has already revealed a large amount of new physics and potential in broad applications. As the semiconductor industry is fast approaching its limits for further performance improvements based on current silicon technologies,(following the so called 'Moore's law), there is a constant search for new, nontraditional materials. Graphene is quite different from conventional semiconductors like silicon. Several novel properties make graphene a very promising candidate to replace silicon in emerging nanoscale electronics. Research interest in this material has grown exponentially [1-11]. For instance, the number of publications doubled in 2006 (up to a total of 350 papers according to the ISI citation index). The American Physical Society March meeting 2007 includes eight sessions on this topic. Nature Materials along with other Nature journals have dedicated a web site focusing on this subject. The aim is to highlight recent research achievements in this field [12-14].

1.1.1 Short History

Graphene is a thermodynamically stable material and exists under normal condition. More than 70 years ago, Landau and Peierls predicted that strictly 2D crystals could not exist due to thermal fluctuations in the low-dimensional crystal lattices. These thermal fluctuations would lead to atomic displacements comparable to interatomic distances [15]. A set of experimental observations have strongly supported this argument. In fact, the melting temperature of thin films rapidly decreases as thickness decreases and thus the films become unstable (segregate into islands or decompose) with a typical thickness of tens of atomic layers [14, 16-17]. As a result, atomic monolayers have so far been known only as an integral part of large 3D structures and they are usually grown epitaxially on top of monocrystals with matching crystal lattices [17]. Without a 3D base, 2D crystals were presumed not to exist.

In 2004, scientists successfully separated graphene as a free standing 2D crystal [3]. The resulting 2D graphene has been found to be continuous within a very large range with high crystal quality [7]. Electrons in graphene can travel thousands of nano-meters without any scattering [5].

1.1.2 Unique Properties

Graphene is quite different from conventional semiconductors. Several novel properties make graphene a very promising candidate to replace silicon in future nanoscale electronics:

(a) Electrons pass through silicon in a series of collisions and generate heat. Collisions limit the speed and size of silicon transistors [1]. However, electrons in graphene transport in a ballistic fashion and follows linear I-V characteristic as shown in Fig. 1.4 [3]. This property allows us to design low-power, faster-switching transistors (refer to our later discussion).

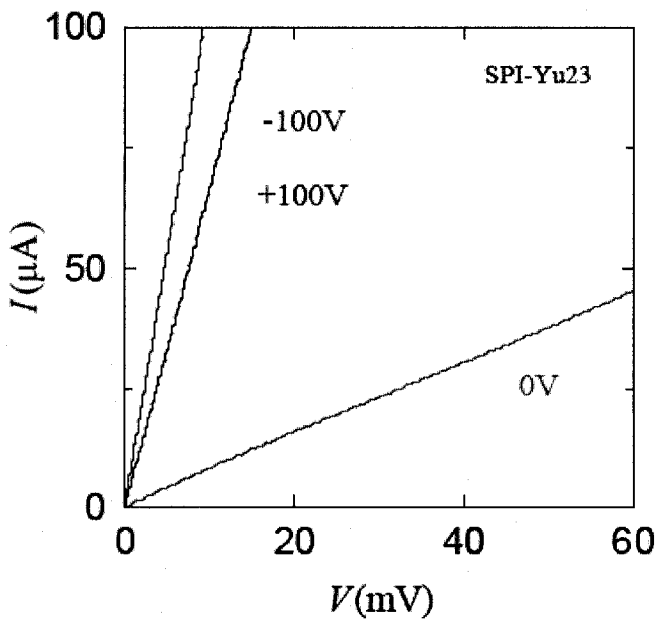

Fig. 1.4: *I-V characteristic of a graphene device with three different gate voltages. Reproduced with permission from K. S. Novoselov et al., Science* ***306****, 666 (2004).*

(b) Flat graphene wafers are easily etched using conventional lithography techniques and they can be cut into continuous graphene nanoribbons to make up electronic circuits. This means that metal wires are no longer needed as connections, which overcomes the major obstacle in the electrical applications of carbon nanotubes [1] since high electric resistances occur when nanotubes are connected with metal wires in an electronic circuit.

(c) Graphene can be tuned to be metallic, semiconducting or even insulating by applying an external gate-voltage or by controlling the width [7-9]. This allows for great flexibility in tailoring the electronic properties in order to build various nanoelectronics devices, e.g., transistors, electric switching and so on.

(d) Electrons in graphene behave like relativistic particles with zero rest mass and have an effective 'speed of light' $c_*=10^6$ m s^{-1} [9] . These two-dimensional Dirac fermions in graphene collectively exhibit a variety of unusual quantum-mechanical phenomena previously thought to occur only in dense plasma around black holes and neutron stars, or in powerful particle accelerators. One typical example is the Klein paradox, in which fast-moving particles pass straight through a seemingly impenetrable barrier [10].

1.1.3 New Physical Phenomena

Electrons in graphene are predicted by the theory and observed in experiments to behave like massless relativistic Dirac Fermions [2, 5, 9-12]. Graphene has also provided a platform for studying 'relativistic' condensed-matter physics or quantum relativistic phenomena, which are unobservable in high-energy physics [14]. Graphene exhibits many new physical phenomena listed as follows.

(a) Linear Energy Spectrum

Graphene's honeycomb lattice is made up of two equivalent carbon sublattices A and B, which leads to the Dirac-like Hamiltonian [5]

$$\hat{H} = \hbar v_F \begin{pmatrix} 0 & k_x - ik_y \\ k_x + ik_y & 0 \end{pmatrix} = \hbar v_F \sigma \bullet k ,$$

where **k** is the quasi-particle momentum, σ is the 2D Pauli matrix. and v_F is the k-independent Fermi velocity. This Hamiltonian generates a linear energy spectrum $E = \hbar v_F k$ within the low energy range near the edges of Brillouin zone ($|E| < 1eV$). This observation is totally different from the parabolic energy spectrum $E = \frac{\hbar^2 k^2}{2m}$ in typical semiconductors. In addition, from the linear relation as shown in Fig. 1.5, we also observe that the valence and conduction bands are symmetrical and touch at the Fermi level E=0, which is called the "Dirac point". This Dirac point leads to the zero energy gap of graphene. However, the density of states is zero at the Dirac point so scientists usually call graphene a zero-gap semi-metal. Therefore, graphene can have partial

characteristics of both metals and semiconductors.

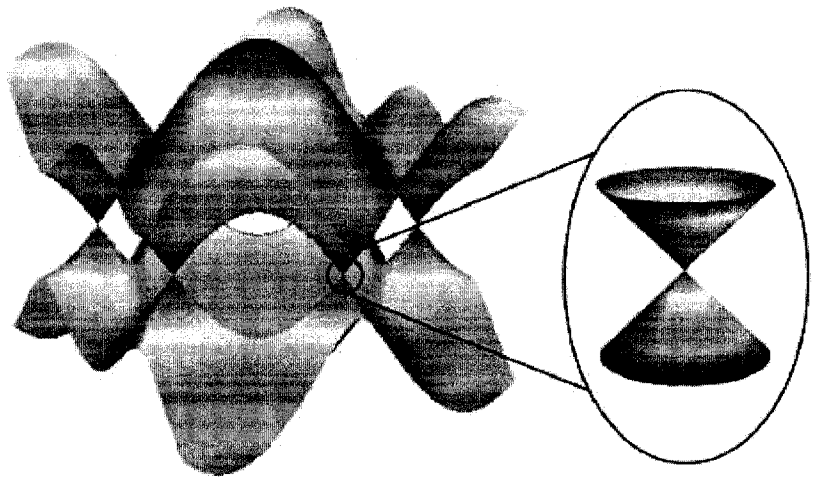

Fig. 1.5: *Band structure of 2D graphene. Its valence and conduction bands touch at the discrete points in the Brillouin zone, and show a semimetal characteristic. The energy momentum dispersion relation becomes linear in the vicinity of those points. Consequently, the electron has zero effective mass.*

(b) Chiral Quantum Hall Effects

In the early stages of graphene research, the main research has been focused on the electronic properties of graphene, researchers attempted to understand graphene's Dirac-like spectrum. Among spectacular phenomena observed in graphene so far, there are two new 'chiral' quantum Hall effects (QHEs): (i) minimum quantum conductivity in the limit of a zero concentration of charge carriers and (ii) the strong suppression of quantum interference effects [14]. These two phenomena have never been reported in condensed matter materials. Fig. 1.6

shows the QHE behavior in graphene, which is a relativistic analogue of the conventional integer QHE. From this figure, we can observe that a continuous ladder of equidistant steps in the Hall conductivity passes through the Dirac point, where charge carriers change from electrons to holes. However, if we look closely we can find that the sequence of Hall conductivity in graphene is shifted by ½ with respect to the standard QHE sequence. Therefore, this QHE has been named as 'half-integer' QHE to reflect both the shift and the fact that it is still a kind of QHE. This anomalous phenomenon is now well understood and it is attributed to the QED-like quantization of graphene's electronic spectrum in magnetic field B. The existence of a quantized energy level at zero E, as shown in the right subfigure in Fig. 1.6, leads to the ½ (non-zero) plateau at E=0.

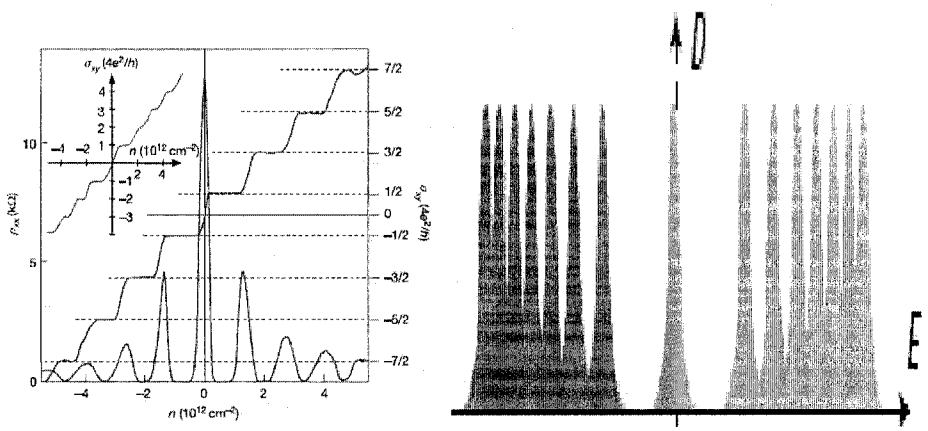

Fig. 1.6: *Chiral quantum Hall effects. Left subfigure, the hallmark of massless Dirac fermions is QHE plateaux in* σ_{xy} *at half integers of* $4e^2/h$. *Right subfigure, Landau quantization in graphene, the sequence of Landau levels in the density of states D is described by* $E_N \propto \sqrt{N}$ *for massless Dirac fermions in graphene.*

*Reproduced with permission from A. K. Geim, and K. S. Novoselov, Nature Mater. **6**, 183 (2006).*

(c) Klein Paradox

Klein Paradox [10, 18-19] was firstly proposed by the Swedish physicist, Oskar Klein, in 1929. He predicted that a relativistic particle can completely pass through a potential barrier without any reflection, even when the height of the barrier exceeds twice of the particle's rest energy. This paradox contradicts our intuition and cannot be explained based on the quantum mechanics either. According to the quantum tunneling theory, electrons in conventional semiconducting materials should bounce back when it hits the barrier, or at least tunnel through the barrier with transmission coefficient exponential decay with the increasing height or the width of the barrier. However, recently, graphene has been predicted to be an effective medium where relativistic quantum tunneling described by the Klein paradox can be tested experimentally [10]. As shown in Fig. 1.7, conduction electrons with energy E can tunnel through a barrier V_0 when valence band shifts upwards. Theoretical results show that under resonance conditions,

$q_x D = \pi N, N = 0, \pm 1, ...$

the barrier becomes transparent (T=1) even when barriers $|V_0| \gg E$ as shown in Fig. 1.8.

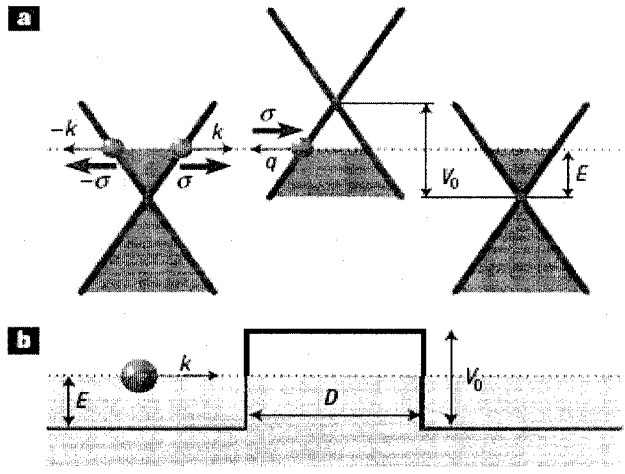

Fig. 1.7: *Tunneling process through a potential barrier in graphene. Reproduced with permission from M. I. Katsnelson, K. S. Novoselov, and A. K. Geim, Nature Physics* **2**, *620 (2006).*

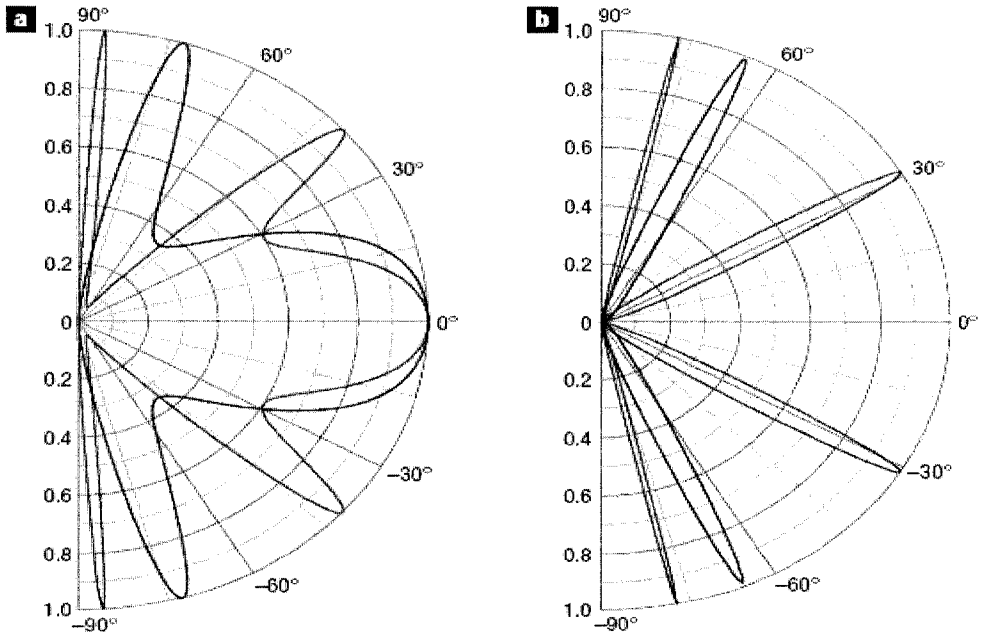

Fig. 1.8: *Klein-like quantum tunneling in graphene systems.* ***a,b****, Transmission probability T through a 100-nm-wide barrier as a function of the incident angle*

*for single- (**a**) and bi-layer (**b**) graphene. The barrier heights V0 are (**a**) 200 meV and (**b**) 50 meV (red curves) and (**a**) 285 and (**b**) 100meV (blue curves). Reproduced with permission from K. S. Novoselov et al., Science **306**, 666 (2006).*

1.1.4 Electronic Devices

Creating novel graphene-based electronic devices is attracting lots of research interest. Companies, such as Intel and IBM, fund research in this area. These companies are actively looking for new nanomaterials to replace silicon-based technology because they foresee that semiconducting material is fast approaching its fundamental limits. Graphene has great potential for future nanoelectronics due to its high carrier mobility. The mobility can be even higher with increased electric-field-induced concentrations, but chemical doping has little or no effect on the mobility [10, 20]. This phenomenon is equivalent to ballistic transport on a submicrometre scale at 300 K. A ballistic transistor at the room temperature has long been a tantalizing, but elusive goal of electronic engineers. Graphene seems to be a promising material to make the elusion come true.

Graphene-based electronic devices can be constructed by tailoring the conductive graphene sheet, in which various nanoscale structures can be curved to make a pure graphene-based circuitry. The advantage of using a pure graphene-based design is that every electronic components including, transistors and interconnects can be made out of graphene. Next, we will show several typical graphene device designs such as graphene transistors, quantum dot devices and veselago lens.

(a) Graphene Transistors

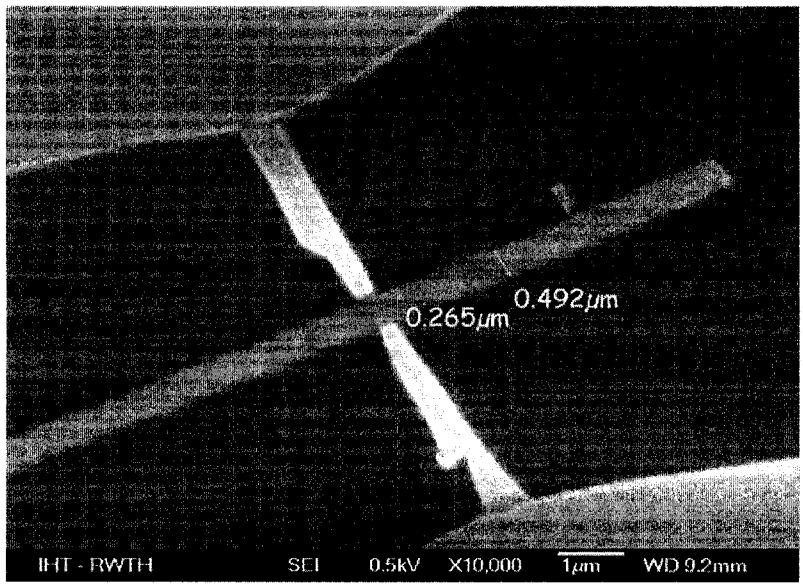

Fig. 1.9: *Scanning electron microscope image of a graphene transistor [21].*

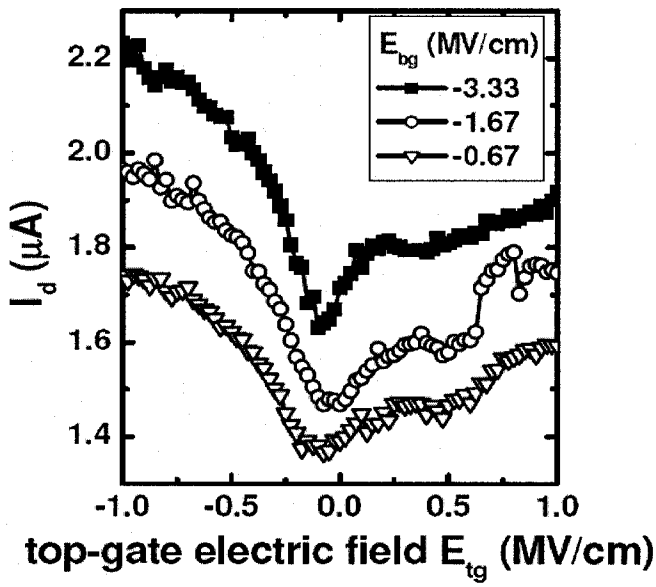

Fig. 1.10: *Top-gate transfer characteristics of the graphene-transistor with different background fields, E_{bg} [21].*

The top-gate transfer characteristics of a graphene transistor are shown in Fig. 1.10 and the drain current I_d is clearly modulated by the top-gate field, E_{bg}. When the negative top-gate fields are increased, a constant increase of hole currents is observed. For positive top-gate fields, there is a distinct plateau between ~0.1 and ~0.4 MV/cm, presumably due to oxide defects.

(b) Graphene Quantum Dot Devices

Fig. 1.11 shows a graphene quantum dot device made entirely of graphene by electron-beam lithography and dry etching. The resulting graphene quantum dot device exhibits very fine characteristics of standard quantum dots including coulomb blockade and single-electron tunneling as shown in the right subfigure of Fig. 1.11. This device, however, can only work at low temperature. Researchers are working hard to extend its operation to the room temperature, which will be practical for real applications.

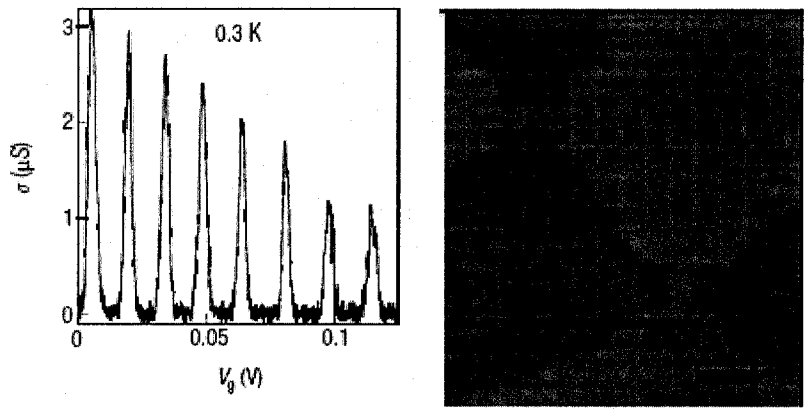

Fig. 1.11: *Coulomb blockade in graphene-quantum dots at low temperature [14]. Left subfigure: Conductance of such devices can be controlled by the back gate. Here, a side electrode is also made out of graphene. Right subfigure: the*

*scanning electron micrograph of two graphene interconnections where quantum dots can be trapped. Reproduced with permission from A. K. Geim, and K. S. Novoselov, Nature Mater. **6**, 183 (2006).*

(c) Veselago Lens

Transparent interfaces between materials are used in optical applications to focus light and thus to manipulate light beams in lenses and prisms. Interfaces like p-n junction (PNJ) in conventional semiconductor devices, however, work differently. For example, a depletion region near the contact between p-type and n-type junctions contains different charge carriers, electrons and holes. Conventional PNJs are, therefore, not suitable to precisely manipulate electron beams. If graphene devices could manipulate light, it would lead to a very interesting discovery [14].

In graphene, researchers have demonstrated that carrier density can be controlled by adjusting the gate voltage [2, 9] or by chemical doping [7]. p-type and n-type graphene strips can therefore be created by applying negative and positive voltages [22] as shown in Fig. 1.12. If we connect the p- and n- strips together, we can create a p-n junction (PNJ). The resulting p-n junction has been demonstrated to be able to focus electric current resembling optical refraction at the surface of metamaterials with negative refractive index [23]. As shown in Fig. 1.13, electrons emitted from a source in a n-type graphene strip transmit through the p-n junction and focus on another point in the p-type graphene strip. When the p-type and n-type strips are symmetric, the distances from the source to the junction and from the drain to the junction are the same. Consequently, the refractive index

is equal to -1. This kind of electron beam focusing resembles the refraction of light in left-handed metamaterials, which also exhibits a -1 refractive index [22-23]. As said by V. V. Cheianov *et al.* in Ref. [22], this finding may be useful for engineers to make electronic lenses and focused beam splitters using the gate-controlled p-n junctions of graphene-based transistors.

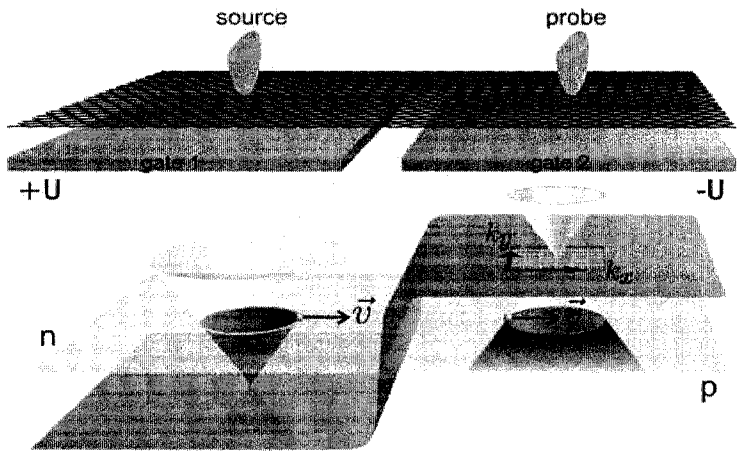

Fig. 1.12: *Graphene p-n junction (PNJ) [22]. Single-layer graphene is placed over a split gate, which is used to create n- (left) and p-doped (right) regions. The energy diagram shows the position of the Fermi level with respect to the touching point of the valence and the conduction bands.*

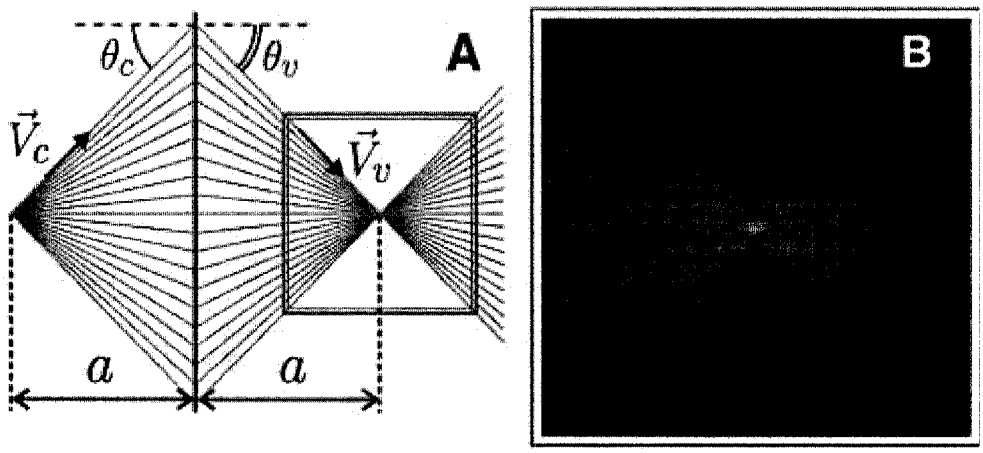

Fig. 1.13: *Focusing of electrons by symmetric PNJ [22]. (A) Charge transmission through a symmetric PNJ. (B) Interference-induced pattern in the charge current near the focal image of the source-contact.*

1.2 Thesis Outline

Although graphene was first reported only three years ago in 2004, remarkably progresses have been made. Only a very tip of an iceberg has been uncovered so far [14]. Large amount of research work are needed in this area to explore more exciting physical and wide-range electrical applications. This thesis focuses on the investigation of fundamental electronic structures and potential applications of graphene nanoelectronics. My contributions described in this thesis consist of three parts: (1) the electronic structures of graphene nanoribbons (Chapters 2), (2) the effect of chemical modifications along carbon bonds at the edge of graphene nanoribbons (Chapter 3), (3) the graphene-based nanodevice (switch, transistor, rectifier) design (Chapter 4-5).

(1) Electronic structure of graphene nanoribbons. In Chapter 2, the analytical solution of the wave function and energy dispersion of armchair graphene nanoribbons (GNRs) will be presented using the tight-binding approximation. The analytical solutions of wave function and associated energy dispersion can be reproduced based on the results of numerical tight-binding method and the the $\boldsymbol{k \cdot p}$ approximation. In addition, we also find that all armchair GNRs with edge deformation have energy gaps, which agrees with the recently reported first-principles calculations.

(2) Chemical modification effect. In Chapter 3, the effects of chemical edge modifications on the structural and electronic properties of GNRs will be discussed. Combination of the first-principle and tight-binding (TB) calculations will be addressed as well. The carbon-carbon (C-C) bond lengths and bond angles near GNR edge considerably change when edge carbon atoms are bounded to different atoms. By introducing a phenomenological hopping parameter $t1$ for nearest-neighbor hopping to represent various chemical edge modifications, we investigated the electronic structural changes of nanoribbons with different widths based on the tight-binding scheme. Theoretical results show that addends (absorption of atoms to carbon atoms on the edge) can alter the band structures of armchair GNRs and even result in observable metal-to-insulator transition.

(3) Graphene-based nanodevices. In Chapter 4, an armchair graphene

nanoribbon switch, which can manifest the Klein paradox, will be discussed. The resulting switch displays an excellent on-off ratio performance. An anomalous tunneling phenomenon, in which electrons do not pass through the graphene nanoribbon junction even when the conventional resonance condition is satisfied, is observed. We proposed a selective tunneling rule to explain this interesting transport behavior. Base on this selective rule, our switch design can also achieve the confinement of electron to form quantum qbit, which is needed to build quantum-dot device.

In Chapter 5, we propose a design of a transmission gate and a field-effect transistor, which are realized by controlling the applied gate voltages in the junction region of GNRs. For the proposed Z-shaped transmission device, electrons across the junction can be rectified according to the external gate bias. The device current-voltage (I-V) characteristics clearly show the amplification effects. The I-V curve is also asymmetric with respect to the bias polarity, which indicates that this device can work as either an n-type or a p-type transistor by changing the polarity of gate bias without doping.

Chapter 2

Electronic Structures of Graphene Nanoribbons

In this chapter, we will discuss the electronic structures of GNRs in detail. The research was jointly performed by Zhengfei Wang and me supervised by Dr. Jie Chen and Dr. Qinwei Shi at University of Alberta in Dec. 2006, The results have been published in Phys. Rev. B 75, 165414 (2007). These structures are simple variations of two-dimensional graphene. In Section 2.1, we will provide a classification method of GNRs according to their geometric structure at the edges of ribbons. We will then address the analytical results of wavefunction and energy spectrum of GNRs in Section 2.2.

2.1 Geometric Structure of GNRs

There are two typical edge shapes for GNRs, namely armchair or zigzag as shown in Fig. 2.1. The real edge structure, however, is irregular and complicated [24]. For simplicity, the general edges of GNRs can be described as the mixtures of both armchair and zigzag edges. A two-dimensional infinite graphene sheet can

be cut along the armchair edge (red arrow in x axis) and the zigzag edge (blue arrow in y axis) to obtain two typical kinds of graphene nanoribbons: armchair and zigzag GNRs, respectively. The ribbon width *n* denotes the number of dimer lines for an armchair GNR or the number of zigzag lines for a zigzag GNR as shown in Fig. 2.1. The unit cell of armchair and zigzag GNRs are shown in the rectangular boxes.

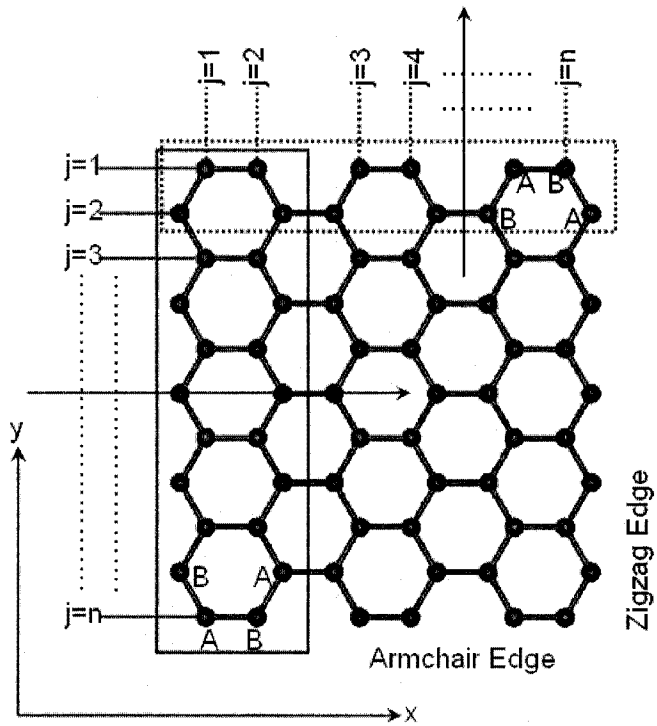

Fig. 2.1: *Geometric structure of GNRs with armchair and zigzag edges.*

2.2 Analytical Wave Function and Energy Spectrum of Armchair GNRs

The analytical wave function and energy dispersion of zigzag nanoribbons were

derived by several research groups [25-26]. For armchair GNRs, the analytical forms of wave functions within the low-energy range have been derived based on the effective-mass approximation [27]. It is predicted that all zigzag GNRs are metallic with localized states on the edges [24-26, 28], while armchair GNRs are either metallic or insulating, depending on their widths [24, 28]. To date, there is no general expression of the wave function in armchair GNRs. In this section, we derive a general analytical expression of wave function and eigenenergy in armchair GNRs applicable to various energy ranges. In Section 2.2.1, we focus on perfect armchair GNRs without any edge deformation and derive the energy dispersion by imposing the hard-wall boundary condition. Due to the quantum confinement, the spectrum breaks into a set of subbands and the wave vector along the confined direction becomes discretized, which is similar to the case of carbon nanotubes [29]. We observe that the electronic structure of perfect armchair GNRs strongly depends on the width of the ribbon. The system, for instance, is metallic when $n=3m+2$ and is insulating otherwise, where m is an integer. Furthermore, we study the low-energy electronic structure. The linear dispersion relation is observed in armchair GNRs. In Section 2.2.2, we evaluate the effect of deformations on the edges on the electronic structure of armchair GNRs. Calculation results based on the derived analytical wave function show that all armchair GNRs have nonzero energy gaps due to the variation of hopping integral near the edges. This observation is in line with the recently reported first-principles calculations [30].

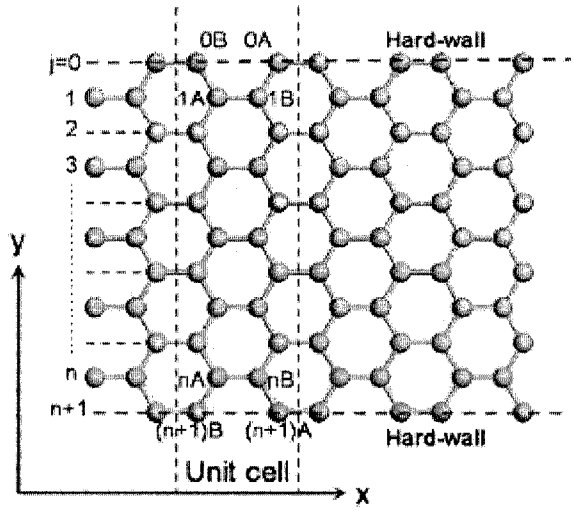

Fig. 2.2: *Structure of an armchair graphene nanoribbon, consisting of sublattices A and B. The width of the armchair GNR is n. Every unit cell contains n numbers of A and B sublattices. Two additional hard walls (j=0, n+1) are imposed on both edges.*

2.2.1 Perfect Armchair GNRs

The structure of armchair GNRs consists of two types of sublattices A and B as illustrated in Fig. 2.2. The unit cell contains n A-type atoms and n B-type atoms. Based on the translational invariance, we choose the plane-wave basis along the x direction. Within the tight-binding model, the wave functions of A and B

sublattices can be written as

$$|\psi\rangle_A = \frac{1}{N_A}\sum_{i=1}^{n}\sum_{x_{A_i}} e^{ik_x x_{A_i}}\phi_A(i)|A_i\rangle,$$
$$|\psi\rangle_B = \frac{1}{N_B}\sum_{i=1}^{n}\sum_{x_{B_i}} e^{ik_x x_{B_i}}\phi_B(i)|B_i\rangle, \tag{2.1}$$

where $\phi_A(i)$ and $\phi_B(i)$ are the components for A and B sublattices in the y direction, which is perpendicular to the edge. $|A_i\rangle$ and $|B_i\rangle$ are the wave functions of the pz orbit of a carbon atom located at A and B sublattices, respectively. To solve $\phi_A(i)$ and $\phi_B(i)$, we employ the hard-wall boundary condition

$$\phi_A(0) = \phi_B(0) = 0,$$
$$\phi_A(n+1) = \phi_B(n+1) = 0. \tag{2.2}$$

Choosing $\phi_A(i) = \phi_B(i) = \sin(\frac{\sqrt{3}q_y a}{2} i)$ and substituting them into Eq. (2.2), we get

$$q_y = \frac{2}{\sqrt{3}a}\frac{p\pi}{n+1}, \quad p = 1,2,...,n. \tag{2.3}$$

q_y is the discretized wave vector in the y direction and a=1.42 Å is the bond length between carbon atoms. To obtain the normalized coefficients, N_A and N_B, we introduce the normalization condition

$${}_A\langle\psi|\psi\rangle_A = {}_B\langle\psi|\psi\rangle_B = 1. \tag{2.4}$$

It is straightforward to obtain $N_A = N_B = \sqrt{\frac{N_x(n+1)}{2}}$, where N_x is the number of unit cells along the x direction. The total wave function of the system can be

constructed by the linear combination of $|\psi\rangle_A$ and $|\psi\rangle_B$,

$$|\psi\rangle = C_A\left[\sqrt{\frac{2}{N_x(n+1)}}\sum_{i=1}^{n}\sum_{x_{A_i}} e^{ik_x x_{A_i}} \sin(\frac{\sqrt{3}q_y a}{2} i)|A_i\rangle\right] + C_B\left[\sqrt{\frac{2}{N_x(n+1)}}\sum_{i=1}^{n}\sum_{x_{B_i}} e^{ik_x x_{B_i}} \sin(\frac{\sqrt{3}q_y a}{2} i)|B_i\rangle\right]$$

(2.5)

Under the tight-binding approximation, the Hamiltonian of the system is

$$H = \sum_i \varepsilon_i |i\rangle\langle i| - \sum_{\langle i,j\rangle} t_{i,j} |i\rangle\langle j|, \tag{2.6}$$

where $\langle i,j\rangle$ denotes the nearest neighbors.

In perfect armchair GNRs, we set $t_{i,j} = t$ and $\varepsilon_i = \varepsilon$ for simplicity. By Substituting Eqs. (2.5) and (2.6) into the Schrodinger equation, we can easily obtain the following matrix expression:

$$\begin{pmatrix} \varepsilon & \mu \\ \mu^* & \varepsilon \end{pmatrix}\begin{pmatrix} C_A \\ C_B \end{pmatrix} = E\begin{pmatrix} C_A \\ C_B \end{pmatrix}, \tag{2.7}$$

where $\mu = {}_A\langle\psi|H|\psi\rangle_B = -t\left[2e^{ik_x a/2}\cos(\frac{\sqrt{3}a}{2}q_y) + e^{-ik_x a}\right]$.

Solving Eq. (2.7), we get the energy dispersion and wave function as

$$E = \varepsilon \pm |\mu|,$$
$$|\psi\rangle_{\pm} = \frac{\sqrt{2}}{2}\left(|\psi\rangle_A \pm \sqrt{\frac{\mu^*}{\mu}}|\psi\rangle_B\right). \tag{2.8}$$

Here, $\pm$ denotes the conduction and valance bands, respectively. $-\frac{\pi}{2} \le \frac{3k_x a}{2} \le \frac{\pi}{2}$ is required within the first Brillouin zone (BZ). These results are valid for various

energy ranges.

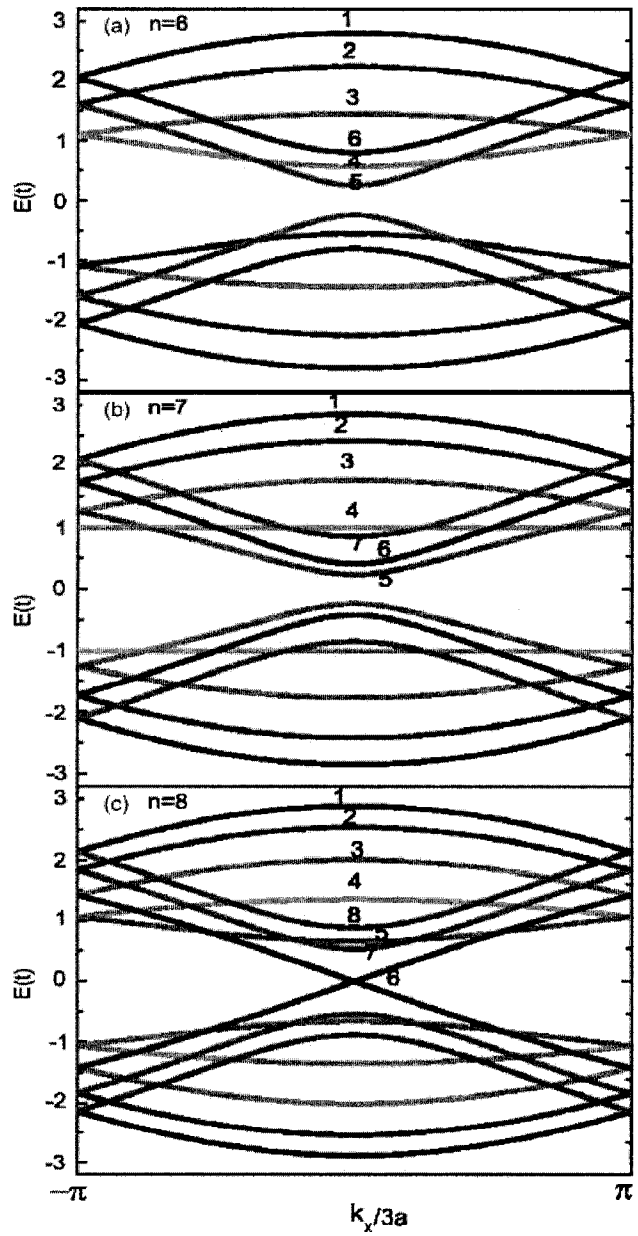

Fig. 2.3: *Electronic structures of perfect armchair GNRs with various widths, (a)*

n=6, (b) n=7, and (c) n=8, respectively. The wave vector is normalized based on the primitive translation vector of individual GNRs. The value of p for each subband is labeled in the figure.

Fig. 2.3 shows the energy dispersion for perfect armchair GNRs with width n=6, 7 and 8. Here, we set ε=0. The results are the same as those obtained by using the numerical tight-binding method. The electronic structures of armchair GNRs depend strongly on their widths. When n=8, the lowest conduction band and the upmost valence band touch at the Dirac point, which leads to the metallic behavior of n=8 armchair GNRs. Armchair GNRs, however, are insulating when n=6 and n=7. Armchair GNRs with the width of n =3m+2 (m is an integer) are generally metallic and otherwise are insulating [24, 27].

In addition, we observe several interesting features in the band structures of armchair GNRs.

(i) A flat conduction or valence band (p=4) exists, if n=7 as shown in Fig. 2.3 (b). Such a flat band generally corresponds to $\frac{p}{n+1}=\frac{1}{2}$ or equivalently $\cos\frac{p\pi}{n+1}=0$. The energy dispersion becomes independent of k_x and the eigenenergy always equals $\pm t$. A flat band, in general, exists only when n is odd.

(ii) The subbands can be labeled by the quantum number p. Together with the wave number k_x, the quantum number p can be used to define the chirality of the electrons in quasi-one-dimensional (1D) graphene ribbons similar to that in 2D graphene. To identify different subbands, we need the quantum number p_i of the i^{th} conduction or valence band. Here, the definition of the sequence of subbands is referred to as the value of eigenenergy E_C in the center of first Brillouin zone ($k_x = 0$),

$$E_C = \pm t \left| 2\cos\frac{p\pi}{n+1} + 1 \right|. \tag{2.9}$$

For the metallic armchair GNRs with width n=3m+2, when $\frac{p\pi}{n+1} = \frac{2\pi}{3}$ or equivalently p=2m+2, the energy gap between conduction and valence bands is zero. Therefore, $p_1 = 2m+2$ corresponds to the first conduction or valence band in n=3m+2 GNRs. For the second conduction or valence bands, E_C should have the minimal nonzero value compared to the third or even higher band. After analyzing the value of E_C, we find that $p_2 = 2m+3$, $p_3 = 2m+1$ for metallic armchair GNRs (n=3m+2). By similar analysis, for $n > 10$, we can obtain $p_1 = 2m+1$, $p_2 = 2m$, $p_3 = 2m+2$ for n=3m armchair GNRs and $p_1 = 2m+1$, $p_2 = 2m+2$, $p_3 = 2m$ for n=3m+1 armchair GNRs, respectively. For all subbands, there is no general rule of the subband index p.

(iii) Lots of research interest has been focusing on the energy dispersion and

wave function of 2D graphene and 1D GNRs within the low-energy range [9, 27, 30]. Low-energy electrons behave as massless relativistic particles in a 2D infinite graphene system [2-3, 9-10, 27]. Whether electrons keep their relativistic property when they are confined in quasi-1D graphene nanoribbons is an interesting issue. In what follows, we will focus on the expansion of our analytical expressions to the low-energy limit. When $\frac{p\pi}{n+1} \to \frac{2}{3}\pi$ and $\frac{3k_x a}{2} \to 0$, we rewrite the eigenenergy in Eq. (2.8) as

$$E \approx \pm\frac{3}{2}at\sqrt{k_x^{\,2} + \tilde{q}_y^{\,2}} = \pm\hbar v_F k, \tag{2.10}$$

where $\tilde{q}_y(p) = \frac{2}{\sqrt{3}a}\left(\frac{p\pi}{n+1} - \frac{2}{3}\pi\right)$, $k^2 = k_x^{\,2} + \tilde{q}_y^{\,2}$, p is the subband index. This low-energy expansion generates the $E \propto k$ linear dispersion, with Fermi velocity $v_F = \frac{3at}{2\hbar} \approx 10^6 (ms^{-1})$. This expression reproduces the result of $\boldsymbol{k}\cdot\boldsymbol{p}$ approximation [27]. Note that the wave vector in the confined direction ($\tilde{q}_y$) is discretized, corresponding to different subbands. What is worthy of mentioning is that this energy dispersion works well only at the low-energy limit. By substituting the value of p_1 into Eq. (2.10), we get the low-energy expansion of the first conduction or valence band for armchair GNRs as

$$E_1(3m) \overset{k_x \to 0}{\approx} \pm\frac{3}{2}at\sqrt{k_x^{\,2}+\left(\frac{2\pi}{3\sqrt{3}(3m+1)a}\right)^2},$$

$$E_1(3m+1) \overset{k_x \to 0}{\approx} \pm\frac{3}{2}at\sqrt{k_x^{\,2}+\left(\frac{2\pi}{3\sqrt{3}(3m+2)a}\right)^2},$$

$$E_1(3m+2) \overset{k_x \to 0}{\approx} \pm\frac{3}{2}atk_x,$$

(2.11)

Fig. 2.4 shows the quality of low-energy approximation. For large width armchair GNRs, low-energy approximation seems to work well except at the edge of first Brillouin zone. As the width gets larger, the quantum confinement due to the edge becomes less important and the 1D nanoribbon tends to behave like 2D graphene. For large n, as expected, the band structure generates the linear dispersion relationship, $E \propto k$, in the low-energy limit.

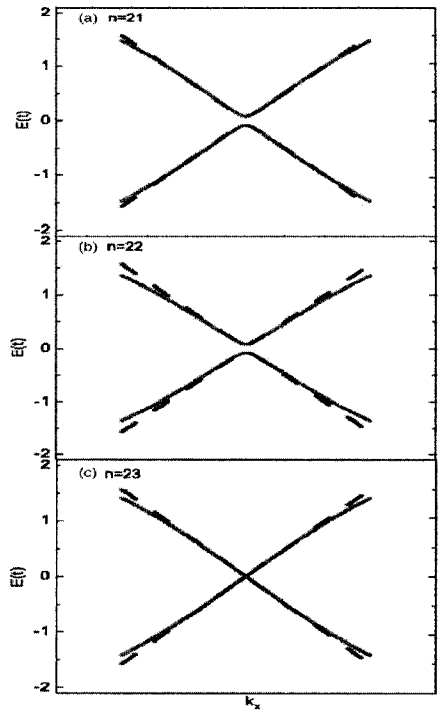

Fig. 2.4: *The first conductance and valence bands within the first Brillouin zone: exact solutions from Eq. (2.8) (red solid line) and low-energy approximation from Eq. (2.11) (blue dash line) for armchair GNRs with various widths, (a) n=21, (b) n=22, (c) n=23, respectively. The wave vector is normalized based on the primitive translation vector of individual GNRs.*

In addition, from the expression of the wave function, we also obtain the local density of electronic states in perfect armchair GNRs, $P_A(i) = P_B(i) \propto \sin^2\left(\frac{p\pi}{n+1} i\right)$. Fig. 2.5 shows the squared wave functions of the lowest conduction band at the center of first Brillouin zone. Note that Figs. 2.5 (a) and 2.5 (c) reproduce the results of the $\boldsymbol{k \cdot p}$ approximation [27]. The state density

oscillates as a function of the lattice position. The oscillation period is related to $\frac{n+1}{p}$. For n=3m+2 armchair GNRs, the oscillation period is just 3, which is shown clearly in Fig. 2.5 (a). For n=3m, 3m+1 armchair GNRs, we should write $\frac{n+1}{p}$ into irreducible form $\frac{\alpha}{\beta}$. The oscillation period is then α, which is the numerator of the irreducible form of $\frac{n+1}{p}$. To match the results presented in Ref. [27], we choose n=51 and n=52 as an example. We get $\alpha = 51$ and $\alpha = 52$, respectively. As shown in Figs. 2.5 (b) and 2.5 (c), the oscillation period of state density for n=51 and n=52 armchair GNRs equals their width.

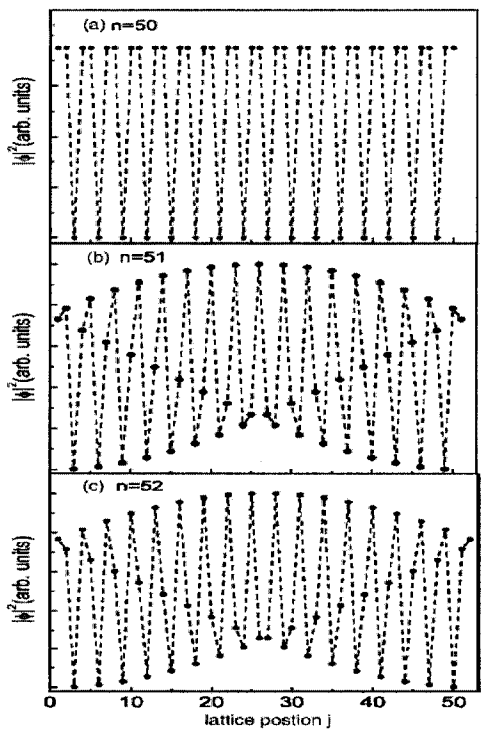

Fig. 2.5: *Local density of the states in the first conduction or valence band at*

$k_x = 0$ for armchair GNRs with various widths, (a) n=50, (b) n=51, and (c) n=52, respectively (n is so chosen to match the results in Ref. [27]).

2.2.2 Energy Gap and Wave Function for Edge-deformed GNRs

Because every atom on the edge has one dangling bond unsaturated, the characteristics of the *C-C* bonds at the edges can change GNRs' electronic structure dramatically [31-32]. To determine the bandgaps of GNRs on the scale of nanometer, edge effects should be considered. The change of edge bond length and angle can lead to considerable variations of electronic structure, especially within the low-energy range [30, 33]. In previously reported work, the edge carbon atoms of GNRs are all passivated by hydrogen atoms or other kinds of atoms or molecules [27, 30-33]. The bonds between hydrogen and carbon are different from those *C-C* bonds. Accordingly, the transfer integral of the *C-H* bonds and onsite energy of carbon atoms at the edges are expected to differ from those in the middle of GNRs. The bond lengths between carbon atoms at the edges are predicted to vary about 3–4% when hydrogenated [30]. Correspondingly, the hopping integral increases about 12% extracted from the analytical tight-binding expression [30, 34]. To evaluate the effect of various kinds of edge deformation, we carried out general theoretical calculation and analysis with our analytical solution of armchair GNRs. In general, we can set the variation of the transfer integral and on-site energy as $\delta_{i,j}$, ε_i for the i^{th} *A*-type or

B-type carbon atom. The Hamiltonian of the GNRs with deformation on the edge can be rewritten as

$$H = \sum_i \varepsilon_i |i\rangle\langle i| - \sum_{\langle i,j \rangle} (t + \delta_{i,j}) |i\rangle\langle j|. \tag{2.12}$$

The energy dispersion and wave function are readily obtained by solving the Schrodinger equation with the perturbation approach

$$\begin{aligned} E &= \gamma \pm |\mu + \delta\mu|, \\ |\psi\rangle_{\pm} &= \frac{\sqrt{2}}{2}\left(|\psi\rangle_A \pm \sqrt{\frac{(\mu+\delta\mu)^*}{\mu+\delta\mu}} |\psi\rangle_B \right). \end{aligned} \tag{2.13}$$

where $\gamma = \frac{2}{n+1}\sum_{i=1}^{n} \varepsilon_i \sin^2\left(\frac{p\pi}{n+1} i\right)$ is the energy shift originating from the variation of on-site energy, while the shift from the hopping integral variation is

$$\begin{aligned} \delta\mu = & -\frac{2}{n+1}\sum_{i=1}^{n} \left[\delta_{t_{i(A)i(B)}} \sin^2\left(\frac{p\pi}{n+1} i\right) e^{-ik_x a} \right. \\ & + \delta_{t_{i(A)i-1(B)}} \sin\left(\frac{p\pi}{n+1} i\right) \sin\left(\frac{p\pi}{n+1}(i-1)\right) e^{ik_x a/2} \\ & \left. + \delta_{t_{i(A)i+1(B)}} \sin\left(\frac{p\pi}{n+1} i\right) \sin\left(\frac{p\pi}{n+1}(i+1)\right) e^{ik_x a/2} \right] \end{aligned} \tag{2.14}$$

Such a general expression could include various kinds of small edge deformations, ranging from the quantum confinement effect due to the finite width, to the effect of saturated atoms or molecules attached to edge carbon atoms. This result shows that the deformation leads to a considerable deviation of the energy dispersion relation and wave function of the deformed system from those

in perfect armchair GNRs. The local density of states on both kinds of sublattices, however, remains the same as that in perfect armchair GNRs. The reason is that the wave functions of sublattices A and B change their relative phases, but keep the magnitudes unchanged. The variations from both the on-site energy and hopping integral contribute to the energy shift, while the change of on-site energy has no contribution to the wave function as shown in Eq. (2.13).

To show the impact caused by structural deformation, we model the deformation by using an exponential distribution function as an example. The hopping variations between i^{th} A and i^{th} B atoms are

$$\begin{aligned} \delta_{t_{i(A)i(B)}} &= \delta t_i = \delta t_0 e^{-\left[L/2-|y(i)|\right]/\rho_L}, \\ \delta_{t_{i(A)i-1(B)}} &= \delta_{t_{i(A)i+1(B)}} = 0, \end{aligned} \tag{2.15}$$

where $y(i) = \frac{\sqrt{3}}{4} a(2j-n-1)$ is the coordinate of the i^{th} atom in the y direction, $L = \frac{\sqrt{3}}{2} a(n-1)$ is the width of the GNRs. The deformation characteristic length ρ_L is used to indicate the extent of the deformation from the edge to the middle of the GNRs. For example, when $\rho_L \to \infty$, $\delta t_i = \delta t_0$ for any i, the deformation is uniform from the edge to the middle; when $\rho_L \to 0$, $\delta t_1 = \delta t_n = \delta t_0$, $\delta t_i = 0$ for $i \neq 1$ or n, the deformation is only localized on the edge bonds [27]. Typically, we set the hopping integral variation δt_0=12%t and the hopping integral of perfect GNRs t=2.7 eV [27]. Our perturbation results are valid only when the deformation is small. For example, we have compared the analytical perturbation

results with those obtained through numerical diagonalization and found the difference becomes quite large when $\delta t_0 > 15\%$ (the energy gaps obtained from both methods differ by more than 10% when $\delta t_0 > 15\%$). For larger deformation, we should employ the numerical diagonalization method or the density functional theory (DFT) to explore the electronic structure of GNRs.

By introducing the deformation, we observe considerable changes of energy gaps compared to those of perfect armchair GNRs as shown in Fig. 2.6. For example, for n=6, 7, 8, the energy gaps are 1.11, 1.54, and 0.22 eV, respectively, when $\rho_L = 0.01L$. They are much larger than those of perfect armchair GNRs (0.49, 0.47, and 0 eV, respectively). All armchair GNRs become semiconducting. The energy gaps between the lowest conduction band and the highest valence band become the function of ribbon width as indicated by three separate curves in Fig. 2.6. When $\rho_L = L$, the energy gaps fluctuate for large n and three curves cross over. When $\rho_L = 0.1L$, the deformation is localized near the GNR edges and the energy gap for n=3m+1 GNR is always larger than those of n=3m and n=3m+2 GNRs. When $\rho_L = 0.01L$, the characteristic length is so small that the deformation is localized along two edges, which has been discussed in Ref. [27].

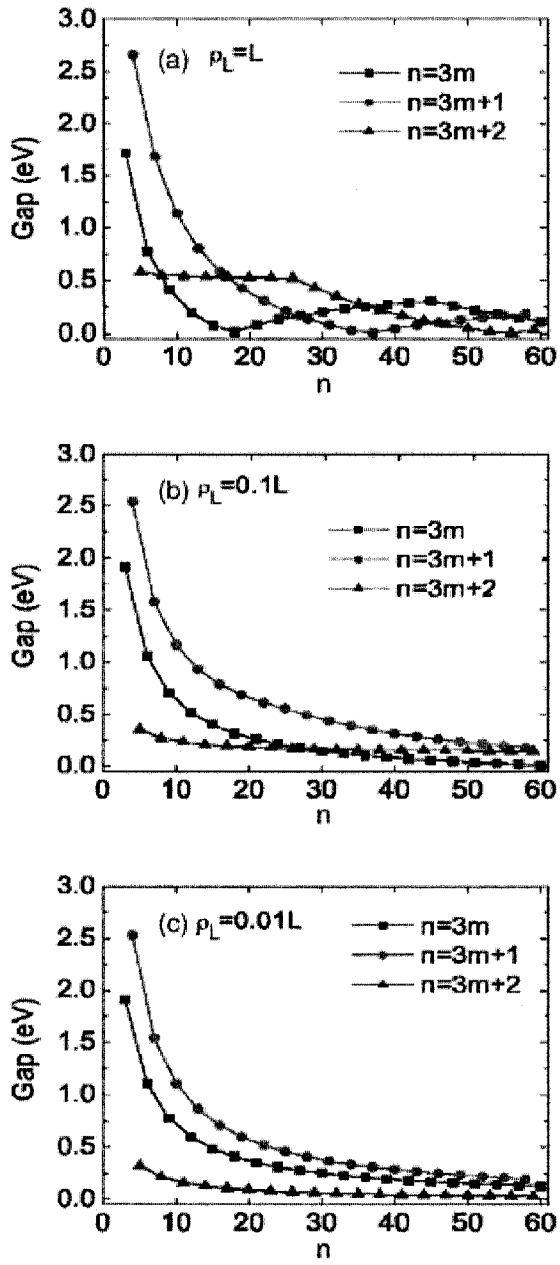

Fig. 2.6: *The energy gaps between the lowest conduction band and the highest valence band as a function of width n with the characteristic length (a)* $\rho_L = L$, *(b)* $\rho_L = 0.1L$, *and (c)* $\rho_L = 0.01L$.

The corresponding energy gaps for different width ribbons are as follows:

$$\begin{aligned}
\Delta_{3m} &= \Delta_{3m}^{0} - \frac{8\delta t}{3m+1}\sin^2\frac{m\pi}{3m+1}, \\
\Delta_{3m+1} &= \Delta_{3m+1}^{0} + \frac{8\delta t}{3m+2}\sin^2\frac{(m+1)\pi}{3m+2}, \\
\Delta_{3m+2} &= \Delta_{3m+2}^{0} + \frac{2\delta t}{m+1},
\end{aligned} \tag{2.16}$$

where Δ_{3m}^{0} , Δ_{3m+1}^{0}, and Δ_{3m+2}^{0} are the energy gaps of perfect armchair GNRs. Their values can be extracted from Eq. (2.9): $2t\left|2\cos\frac{(2m+1)\pi}{3m+1}+1\right|$, $2t\left|2\cos\frac{(2m+1)\pi}{3m+2}+1\right|$, and 0. This result suggests that all armchair graphene ribbons with edge deformation have nonzero energy gaps and are insulators and $\Delta_{3m+1} > \Delta_{3m} > \Delta_{3m+2}$ for any m.

2. 4 Discussion

In this Chapter, we study the electronic states of armchair GNRs analytically. By imposing the hard-wall boundary condition, we find the analytical solution of wave function and energy dispersion in armchair GNRs based on the tight binding approximation. Our results reproduce the numerical tight-binding calculation results and the solutions using the effective-mass approximation. We also derive the low-energy approximation of the energy dispersion, which matches the exact solution except for the edge of first Brillouin zone. The linear energy dispersion is

observed in armchair GNRs in the low-energy limit. In addition, we also evaluate the impact of the edge deformation on GNRs and derive a general expression of wave function and energy dispersion. We can reproduce the energy gap for hydrogenated armchair GNRs presented in Ref. [27]. When we consider the edge deformation, all armchair GNRs have nonzero energy gaps and thus are insulting. Overall, the derived analytical form of the wave function can be used to quantitatively investigate and predict various properties in armchair graphene ribbons.

Chapter 3

Chemical Modification Effects on GNR's Electronic Structures

Zigzag GNRs, which correspond to unwrapped armchair CNTs with zigzag edges, are predicted to be metallic (if the spin degree of freedom is not considered). However, the electronic structure of armchair GNRs depends strongly on the width of GNRs. Among armchair GNRs, only one third of them are metallic. That is to say, GNRs can be made either as metallic or as semiconducting materials by controlling their width or chirality. As each edge carbon atom of GNRs is bounded only to two neighboring carbon atoms, a dangling carbon bond can determine the electronic properties of GNRs.

This part of research has been done by Zhengfei Wang and me under the supervision of Dr. Jie Chen and Dr. Qinwei Shi at University of Alberta in Nov. 2006. We have reported our findings as a journal paper in March 2007 [Phys. Rev. B 75,113406 (2007)]. In this Chapter, we will discuss chemical modification effects on Graphene's electronic structures. The chapter is divided into two sections. First, the theoretical background for the electronic structures of armchair

and zigzag GNRs will be addressed. Second, the combined first-principles and tight-binding theoretical investigations of chemical modification effects will be described.

3.1 Band Structure of Armchair and Zigzag GNRs

In this section, we review the electronic structure of graphene nanoribbons GNRs with armchair and zigzag edges. The definition of armchair and zigzag GNRs has been illustrated in Chapter 2. Fig. 3.1 shows the two basic GNRs that are defined as one-dimensional graphene sheets confined by a pair of parallel armchair (zigzag) edges on both sides. In previously reported studies [24, 27-29], the dangling bonds of GNRs on the two edges are all assumed to be terminated by hydrogen atoms, and the dangling bonds have no contribution to the electronic states near the Fermi level. Employing a tight-binding calculation within the Huckel approximation, the electronic states for GNRs were calculated. In addition, the analytical solutions of electronic states of perfect armchair and zigzag GNRs have also been worked out [14, 27-28, 31-32, 35]. However, a general method to calculate the electronic structures of GNRs with defects and deformation or so-called "exact diagonalization method" is not available. As shown in Fig. 3.1, there are totally $2n$ carbon atoms in a unit cell of GNRs with width n. We start from the Hamiltonian of the system

$$H = \sum_i \varepsilon_i |i\rangle\langle i| - \sum_{\langle i,j \rangle} t_{i,j} |i\rangle\langle j|, \tag{3.1}$$

where $\langle i,j \rangle$ denotes the nearest neighbors, ε_i is the on-site energy of the i^{th} atom, and $t_{i,j}$ is the hopping integral between the i^{th} and j^{th} atoms.

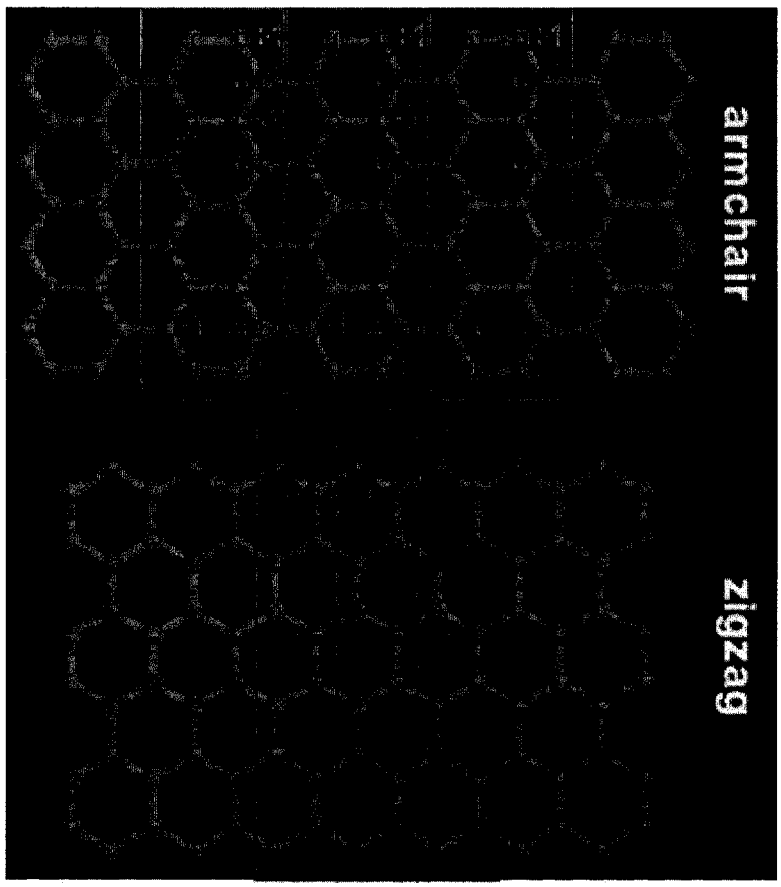

Fig. 3.1: *Atomic structure of armchair and zigzag GNRs. The number of all the atoms in three adjacent unit cells has been labeled for GNRs as width n.*

The wave function of the whole system can be constructed based on the linear combination of atomic orbit (LCAO) method.

$$|\psi\rangle = \frac{1}{\sqrt{N}} \sum_{j} \sum_{i=1}^{n} e^{i\vec{k}\cdot\vec{r}_{ij}} C_i |i\rangle . \tag{3.2}$$

Here, the sum of i is over all the n atoms in a unit cell; the sum of j is over all the unit cells in one-dimensional infinite system. $|i\rangle$ is the atomic orbit of i^{th} atom in the unit cell and C_i is the expansion coefficients. The corresponding Schrodinger equation looks like

$$H|\psi\rangle = E|\psi\rangle. \tag{3.3}$$

By multiplying $\langle 1|$, $\langle 2|$, $\langle 3|$,....., $\langle n+1|$, $\langle n+2|$, $\langle n+3|$,....., $\langle 2n|$ to the left sides of Eq. (3.3) and applying the normalization and orthogonal conditions

$$\langle i|j\rangle = \begin{cases} 1, & i = j \\ 0 & i \neq j \end{cases}$$

$$\langle i|H|j\rangle = \begin{cases} \varepsilon_i, & i = j \\ t_{i,j}, & \langle i,j\rangle \\ 0, & otherwise \end{cases}, \tag{3.4}$$

we can get $2n$ coefficient equations for armchair GNRs

$$\varepsilon_1 C_1 + e^{i\vec{k}\bullet(\vec{r}_2-\vec{r}_1)} t_{1,2} C_2 + e^{i\vec{k}\bullet(\vec{r}_{n+1}-\vec{r}_1)} t_{1,n+1} C_{n+1} = EC_1,$$

$$e^{i\vec{k}\bullet(\vec{r}_1-\vec{r}_2)} t_{2,1} C_1 + \varepsilon_2 C_2 + e^{i\vec{k}\bullet(\vec{r}_3-\vec{r}_2)} t_{2,3} C_3 + e^{i\vec{k}\bullet(\vec{r}_{n+2}-\vec{r}_2)} t_{2,n+2} C_{n+2} = EC_2,$$

$$e^{i\vec{k}\bullet(\vec{r}_2-\vec{r}_3)} t_{3,2} C_2 + \varepsilon_3 C_3 + e^{i\vec{k}\bullet(\vec{r}_4-\vec{r}_3)} t_{3,4} C_4 + e^{i\vec{k}\bullet(\vec{r}_{n+3}-\vec{r}_3)} t_{3,n+3} C_{n+3} = EC_3,$$

•

•

$$e^{i\vec{k}\bullet(\vec{r}_{n-1}-\vec{r}_n)} t_{n,n-1} C_{n-1} + \varepsilon_n C_n + e^{i\vec{k}\bullet(\vec{r}_{2n}-\vec{r}_n)} t_{n,2n} C_{2n} = EC_n,$$

$$e^{i\vec{k}\bullet(\vec{r}_1-\vec{r}_{n+1})} t_{n+1,1} C_1 + \varepsilon_{n+1} C_{n+1} + e^{i\vec{k}\bullet(\vec{r}_{n+2}-\vec{r}_{n+1})} t_{n+1,n+2} C_{n+2} = EC_{n+1},$$

$$e^{i\vec{k}\bullet(\vec{r}_2-\vec{r}_{n+2})} t_{n+2,2} C_2 + e^{i\vec{k}\bullet(\vec{r}_{n+1}-\vec{r}_{n+2})} t_{n+2,n+1} C_{n+1} + \varepsilon_{n+2} C_{n+2} + e^{i\vec{k}\bullet(\vec{r}_{n+3}-\vec{r}_{n+2})} t_{n+2,n+3} C_{n+3} = EC_{n+2},$$

•

•

$$e^{i\vec{k}\bullet(\vec{r}_n-\vec{r}_{2n})} t_{2n,n} C_n + \varepsilon_{2n} C_{2n} + e^{i\vec{k}\bullet(\vec{r}_{2n-1}-\vec{r}_{2n})} t_{2n,2n-1} C_{2n-1} = EC_{2n}, \tag{3.5}$$

and zigzag GNRs

$$\varepsilon_1 C_1 + \left[e^{-i\vec{k}\bullet(\vec{r}_{n+1}-\vec{r}_1)} + e^{i\vec{k}\bullet(\vec{r}_{n+1}-\vec{r}_1)} \right] t_{1,n+1} C_{n+1} = EC_1,$$

$$\left[e^{-i\vec{k}\bullet(\vec{r}_3-\vec{r}_2)} + e^{i\vec{k}\bullet(\vec{r}_3-\vec{r}_2)} \right] t_{2,3} C_3 + \varepsilon_2 C_2 + \left[e^{-i\vec{k}\bullet(\vec{r}_{n+2}-\vec{r}_2)} + e^{i\vec{k}\bullet(\vec{r}_{n+2}-\vec{r}_2)} \right] t_{2,n+2} C_{n+2} = EC_2,$$

$$\bullet$$

$$\bullet$$

$$\varepsilon_n C_n + \left[e^{-i\vec{k}\bullet(\vec{r}_{2n}-\vec{r}_n)} + e^{i\vec{k}\bullet(\vec{r}_{2n}-\vec{r}_n)} \right] t_{n,2n} C_{2n} = EC_n,$$

$$\varepsilon_{n+1} C_{n+1} + \left[e^{-i\vec{k}\bullet(\vec{r}_1-\vec{r}_{n+1})} + e^{i\vec{k}\bullet(\vec{r}_1-\vec{r}_{n+1})} \right] t_{n+1,1} C_1 = EC_{n+1},$$

$$\left[e^{-i\vec{k}\bullet(\vec{r}_2-\vec{r}_{n+2})} + e^{i\vec{k}\bullet(\vec{r}_2-\vec{r}_{n+2})} \right] t_{n+2,2} C_2 + \varepsilon_{n+2} C_{n+2} + \left[e^{-i\vec{k}\bullet(\vec{r}_{n+1}-\vec{r}_{n+2})} + e^{i\vec{k}\bullet(\vec{r}_{n+1}-\vec{r}_{n+2})} \right] t_{n+1,n+2} C_{n+1} = EC_{n+2},$$

$$\bullet$$

$$\bullet$$

$$\varepsilon_{2n} C_{2n} + \left[e^{-i\vec{k}\bullet(\vec{r}_n-\vec{r}_{2n})} + e^{i\vec{k}\bullet(\vec{r}_n-\vec{r}_{2n})} \right] t_{2n,n} C_n = EC_{2n}.$$

(3.6)

We rewrite Eq. (3.5) and Eq. (3.6) using the matrix form for armchair and zigzag GNRs

$$\hat{H} \begin{pmatrix} C_1 \\ \vdots \\ C_{2n} \end{pmatrix} = E \begin{pmatrix} C_1 \\ \vdots \\ C_{2n} \end{pmatrix}. \tag{3.7}$$

We can easily obtain the eigen-energy spectrum of armchair and zigzag GNRs numerically. Fig. 3.2 shows the results of both armchair and zigzag GNRs with width *n=6, 7, 8* to illustrate the energy dispersions. The calculated band structures of armchair ribbons are shown in Fig. 3.2 (a)-(c) for three different ribbon widths. The wave number k is normalized by the primitive translation

vector of each GNR, and the energy E is scaled by the hopping integral t, which is set to 3.0eV. The Fermi level is set to E=0. The top of the valence band and the bottom of the conduction band are located at k=0. It is noticeable that the ribbon width determines whether a GNR is metallic or insulating. As shown in Fig. 3.2 (c), the GNR is metallic when $n=3m+2$, where m is an integer. For the insulating GNRs, which are direct-gap semiconductors, the energy gaps between valence bands and conduction bands decrease with increasing GNR width and they approach to zero as the ribbon width n becomes infinitely large [24].

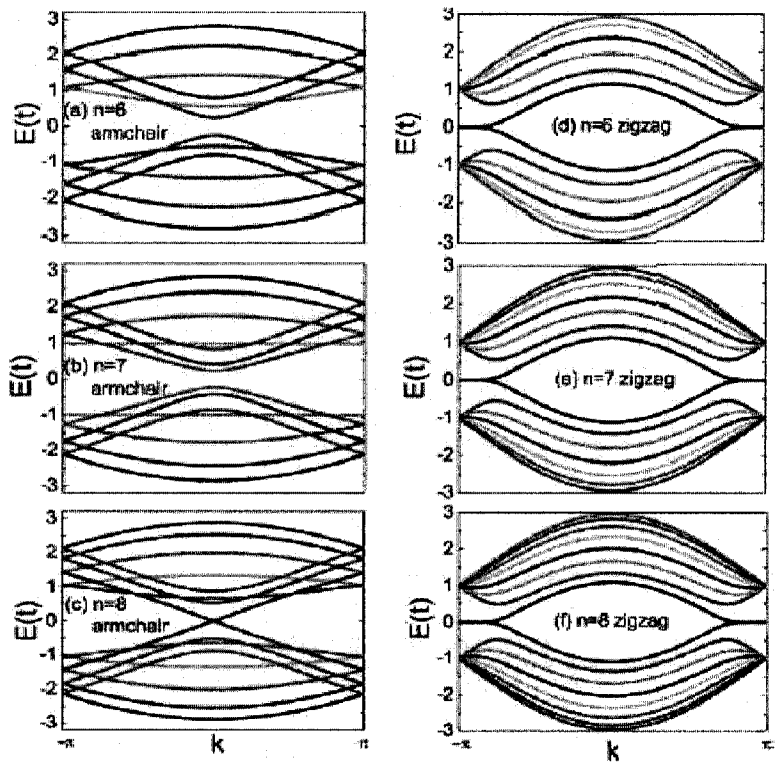

Fig. 3.2: *Band structure of the armchair and zigzag GNRs.*

For zigzag GNRs, a remarkable feature arises in the band structure as shown in Fig. 3.2 (d)-(f). The highest valence band and the lowest conduction band for the zigzag GNRs are always degenerated at $k = \pi$. In addition, a pair of flat bands appears within the range of $2\pi/3 \leq |k| \leq \pi$, where the bands are located closely near the Fermi level. With a detailed examination of charge density distribution, we know that the electronic states in the flat bands correspond to a localized state on the zigzag edges [24]. This kind of localized state originates from the gauge field produced by the lattice deformation [36].

3.2 Chemical Modification Effects

Because each edge carbon atom of GNRs is only bounded to two neighboring carbon atoms, a dangling carbon bond offers a remarkable opportunity to alter the electronic properties of GNRs. This can be done by attaching different atoms or functional molecular groups to the dangling carbon atom. Similar to the functionalization of CNT devices along edge dangling bonds [37-39], the electronic properties of GNRs can also be alternated by chemical edge modifications. In this section, we examine the geometric deformation of finite-width armchair GNRs caused by different edge addends. Our first-principle calculations show that the C-C bond length and bond angle near the edge undergoes observable changes. To include the effect of the deformation on the graphene ribbon edge, we introduce a phenomenological hopping parameter t_1 in

our tight-binding exact diagonalization calculations. Our simulations show that the energy gap depends on ribbon width and hopping parameter t_1. A nonzero energy gap exists for armchair GNRs, which means that the metal-to-insulator transition can be achieved by edge modifications. The increments of C-C bonds and bonding angles at the nanoribbon edge have been reported based on the tight-binding (TB) approximation calculations [40].

We first estimate nanoribbon geometric deformation caused by various chemical addends. For a simple case (each armchair GNR edge carbon atom is saturated by one hydrogen atom), we evaluate geometric and electronic structure changes using the first-principles method. Our optimizations employ the Vienna *ab initio* simulation package [41-42], which is implemented based on the local density approximation [43] of the density functional theory (DFT) [44]. The electron-ion interaction is described by the ultrasoft pseudopotentials [45] and the energy cutoff is set to be 286.6 eV. The atoms' positions are optimized in order to reach the minimum energy with the Hellmann-Feynman forces less than 0.02 eV/Å. The results show that the geometric relaxation localizes near the edge. Only the bond lengths and angles of edge carbon atoms in armchair GNRs have considerable changes compared with those of ideal graphene ribbons. For example, $\angle BAF = 121.6^0$ and $\angle BCD = 118.3^0$. The inter-atomic distance between A and B sites (d_{AB}) of (9, 0) GNR is reduced from 1.42 Å to 1.36 Å, and d_{BC}=1.40 Å d_{CD}=1.40 Å and d_{DE} =1.42 Å, respectively, as shown in Fig. 3.3.

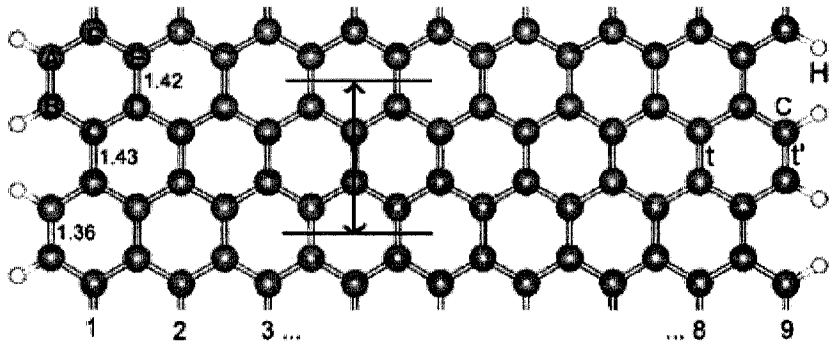

Fig. 3.3: *Optimized structure of a (9, 0) armchair GNR (all edge bonds are bound by hydrogen atoms). Here, the bond length is in Å. Note that a zigzag (n, 0) GNR can be rolled to form an armchair (n, 0) CNT, and an armchair (n, n) GNR can be rolled into a zigzag (n, n) CNT.*

The geometric deformation of armchair GNRs, however, depends on various kinds of chemical addends. For example, if the edge carbon atoms are connected to F atoms, the edge C-C bond lengths are shortened to 1.35 Å (a decrease of about 5%). In general, this kind of geometric deformation results in the changes of hopping parameter between two neighboring carbon atoms on the GNR edge. The parameter change is defined as

$$\Delta t = \frac{\langle 2p_z' | H_1 | 2p_z' \rangle - \langle 2p_z | H_0 | 2p_z \rangle}{\langle 2p_z | \hat{H}_0 | 2p_z \rangle}. \tag{3.8}$$

Here, H_1 and H_0 are the Hamiltonians of the system with and without chemical edge modifications, respectively. $2p_z'$ and $2p_z$ are the atomic orbits of the coupled neighboring carbon atoms at the edge with the optimized bond length and

with the bond length of 1.42 Å, respectively. Our calculations are conducted by using the SIESTA code in real space and single-zeta (SZ) basis [46]. One can expect that the edge hopping parameter can increase (or decrease) as edge C-C distance is shortened (or lengthened). The edge hopping parameter change for the hydrogen-saturated case is predicted to be 10.1% based on the density-functional theory (DFT) method, which is consistent with the numerical result based on the TB approximation [47].

In previous TB approximation calculations [24, 26], the dangling bonds are assumed to be saturated by hydrogen atoms and thus all transfer integrals between the nearest-neighbor sites are set to have the same values. This simple choice of hopping parameter, however, does not consider geometric distortions at the nanoribbon edge. It is important to extend this existing scheme in order to understand the impacts of chemical edge modification on electronic properties of armchair GNRs. For simplicity, we adopt the TB approach to study these impacts. We choose the value of t_1 to be either smaller or larger than the hopping parameter t=2.66 eV of inner C-C bonds to simulate different chemical addends. Our theoretical results show that parameter t_1 itself is sufficient to describe the electronic structure changes of armchair GNRs.

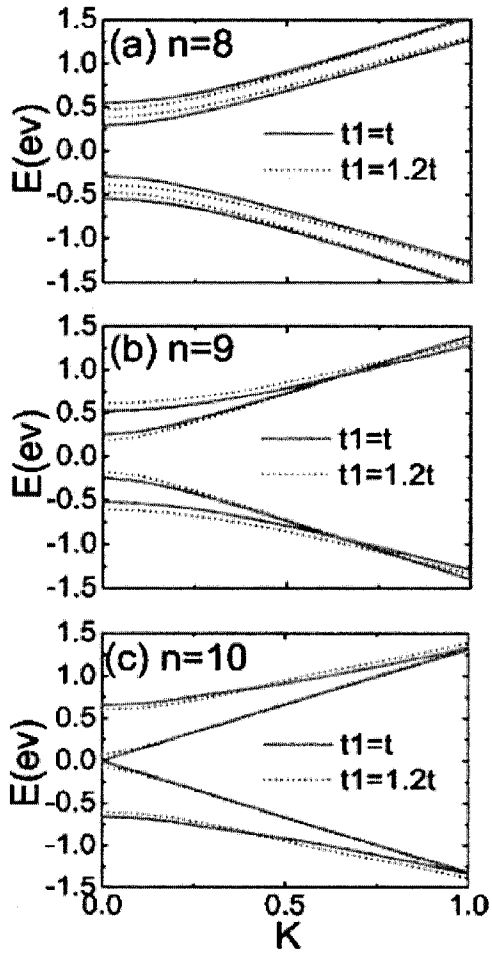

Fig. 3.4: *Top two valence bands and bottom two conduction bands of zigzag GNRs in t_1=t and t_1=1.2t cases.*

Next, we calculate the band structures of armchair GNRs when edge GNR dangling bonds are bounded by atoms or molecular groups. We select ideal armchair GNRs with indices (n, 0) and calculate the band structures of three different ribbon widths (n=8, 9, and 10) by setting t_1=t. The results are shown in Figs. 3.4 (a)-(c) for n=8, 9, and 10 with red solid lines, respectively. For clarity,

we set the Fermi level to zero (E_F=0) and the wave number is normalized by the primitive translation vector for each GNR. In this study, we choose (8, 0), (9, 0), and (10, 0) GNRs (their widths are around 2 nm) as examples to represent (3p+2, 0), (3p, 0), and (3p +1, 0) GNRs (where p is an integer; and they correspond to three different width armchair GNRs labeled with (3p +1, 0), (3p, 0), and (3p+2, 0). It is clear that the band structure of an armchair GNR depends on its width, and the energy gap is 0.58, 0.50, and 0.0 eV for (8, 0), (9, 0), and (10, 0) armchair GNRs, respectively. Armchair GNRs (n, 0) are metallic when n=3p+1 as shown in Fig. 3.4 (c). The energy gaps are nonzero for n=3p and n=3p+2 GNR, in which GNRs become insulating. This result matches the previous reported results [27]. To simulate chemical edge modification effects, t_1 is set to be 1.2t. The π and π^* conduction bands are no longer degenerate at k=0 for a (10, 0) GNR and energy gap becomes 0.14 eV, which leads to metal-to-insulator transition. The DFT results suggest that both quantum confinement and edge effect cause the opening of energy gap [30]. Although (8, 0) and (9, 0) GNRs remain insulating when t_1=1.2t, the energy gap is changed to 0.76 eV (increased) and 0.36 eV (decreased) by changing of the edge hopping parameter. Obviously, these theoretical results show that the electronic property of armchair GNRs is tunable via chemical edge modification.

The band structure of zigzag (n, n) GNRs are similar to those of CNTs except for the existence of edge states that are caused by the gauge field at GNR edges. Due to the localized states at the edges, the uppermost valence band and the lowest conduction band are always degenerated at the Fermi level when

$k_0 \le k \le \pi$. k_0 is slightly less than $2\pi/3$ for finite-width zigzag GNRs. If considering the spin degree of freedom in the DFT calculations, a hydrogen-saturated zigzag GNR is predicted to have a magnetic insulating ground state [30]. By selecting different t_1, we observe that the electronic structure near the Fermi level changes slightly, which indicates that the electronic properties or carrier transport properties of zigzag GNRs are stable and insensitive to the edge modifications.

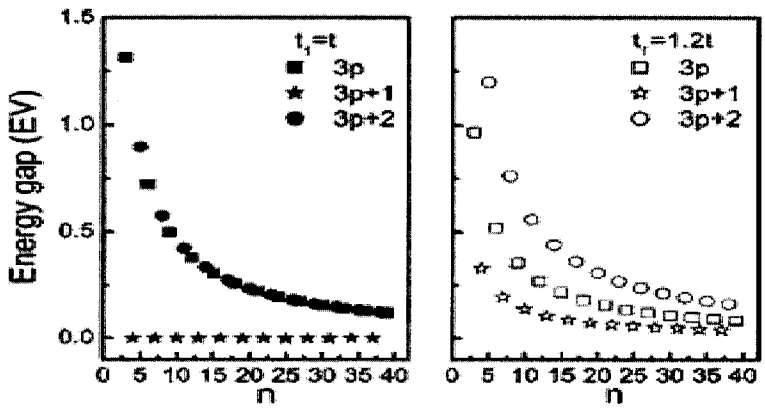

Fig. 3.5: *The energy gap of armchair GNRs depends on their widths: (a) when t_1=t and (b) when t_1=1.2t.*

Fig. 3.5 shows the relationship between armchair GNR widths (n) and their energy gaps when choosing t_1=t and t_1=1.2t. For n=3p, the energy gap of t_1=1.2t is smaller than that of t_1=t. This value decreases when the width increases. For n=3p+1, the energy gap of t_1=t is zero and becomes independent of ribbon width n. For t_1=1.2t, C-C bonds on the edge are shortened and the energy gap opens in

($3p$+1, 0) armchair GNRs. For n=$3p$+2, the energy gaps of t_1=t are nearly the same as that of t_1=1.2t. By comparing the electronic structure of t_1=t with that of t_1=1.2t, we observe that the change of the edge hopping parameter (resulting from the added chemical groups) can significantly affect the electronic properties of armchair GNRs. Our calculations reproduce the results based on the local density approximation of the DFT [30]. It is worth mentioning that the energy gaps of both t_1=t and t_1=1.2t approach zero, or the effect resulting from the addends becomes insignificant when n is very large. This observation suggests that tuning band structure through edge modifications is effective only for finite-width GNR.

Next, we focus on evaluating the energy gap as a function of hopping parameter t_1 for three kinds of armchair GNRs [(8, 0), (9, 0), and (10, 0)]. Results are plotted in Fig. 3.6. It is interesting to note that around t_1=t (representing the slight deformation case), the energy gaps of (8, 0), (9, 0), and (10, 0) armchair GNRs show different trends. In contrast to a (9, 0) GNR, the energy gap of a (8, 0) GNR increases as t_1 increases to around t_1=t. This trend is also observable in Fig. 3.4. A (10, 0) GNR has a zero energy gap at t_1=t. Once we applied chemical edge modifications ($t_1 \neq t$), there is an opened energy gap that always increases no matter whether t1 decreases ($t_1 \leq t$) or increases ($t_1 \geq t$). This result shows that a transition between metallic and insulating GNRs is achievable. Moreover, the energy gap can be controlled by selecting proper addends bounded to the edge carbon atoms of armchair GNRs.

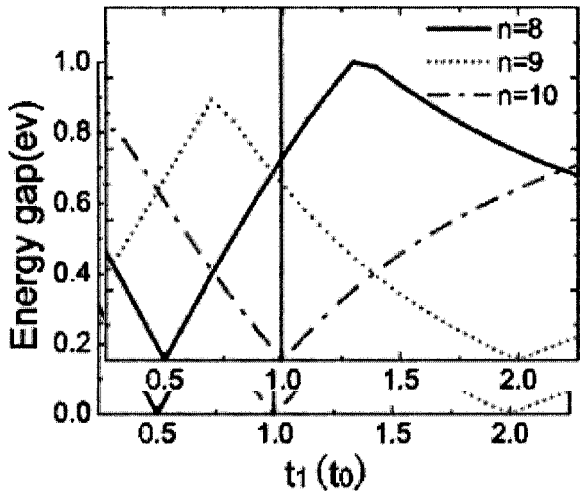

Fig. 3.6: *The effect of hopping parameter t_1 on energy gaps of armchair GNRs with different widths (n=8, 9, and 10).*

In Fig. 3.6, one t_1 value exists that corresponds to the zero energy gap for both (8, 0) and (9, 0) armchair GNRs. This phenomenon shows that, in principle, insulating armchair GNRs can be modified to become metallic GNRs. However, this kind of modification is difficult to implement since the hopping parameter t_1 would have to be reduced or enlarged by 100%.

3. 3 Discussion

In this chapter, the first-principles calculations show that the chemical modification of armchair GNRs results in a considerable deformation of the bond lengths and bond angles near the edge. The introduction of hopping parameter, t_1, using the TB scheme accurately captures the effects caused by chemical edge modifications. Our theoretical results show that addends can change armchair

GNRs' band structures and even lead to observable metal-to-insulator transitions. It should be pointed out that the chemical edge modification is effective only for finite-width GNRs. The study can assist researchers to make graphene-based sensors for detecting various types of molecules attached to GNR's edges.

Chapter 4

Graphene Switch Design –

Illustration of the Klein Paradox

We have designed an armchair GNR switch, which can be used to illustrate the Klein paradox phenomenon. Klein paradox is named after the Swedish physicist Oskar Klein, who proposed this paradox in 1929 to describe the scattering of particles passing through a repulsive potential barrier without decay. This paradox cannot be explained by classical physics. Conventional particles should be reflected completed when the barrier height is larger than particles' incoming energy. Only Dirac particles can penetrate this barrier without any decay even the barrier is very high. In this chapter, our simulation results showed that the Klein paradox exists in graphene nanoribbons. Furthermore, we can use the selective tunneling phenomenon in the Klein paradox to design a novel graphene-based switch. Our resulting switch displays an excellent on-off ratio performance. An anomalous tunneling phenomenon, in which electrons do not pass through the GNR junction even when conventional resonance condition is satisfied, is observed in our numerical simulations. We propose a selective tunneling rule to explain this interesting transport behavior based on our analytical results. Our switch design can also achieve the confinement of electrons and thus serve as the

qubit for quantum computation.

This work was done by Zhengfei Wang and me supervised by Dr. Jie Chen and Dr. Qinwei Shi at University of Alberta in February 2007. This chapter is divided into two sections. Section 4.1 introduces the model and the computation methodology to calculate the conductance in GNRs. Section 4.2 discusses the resulting graphene switch and novel electronic properties.

4.1 Model and Computation Method

In what follows, we consider a semiconducting armchair GNR connected to a left and a right metallic armchair graphene leads. Due to the band gap in our junction, the electron within the energy gap is prohibited to transmit through the junction without applied gate voltage, and the graphene switch stays in the 'off' state. The junction can be turned 'on' when an external gate voltage exceeds a threshold voltage. The applied gate voltage shifts the valence subbands of the graphene nanoribbon upwards to serve as conducting channels. This observation realizes the main feature described by Klein paradox, that is "the electron can pass through a high potential barrier". Here, electrons' incident energy is only 0.05 eV, much lower than the barrier height. The electrons, however, can even pass through the barrier without any decay or the transmission coefficient T=1.

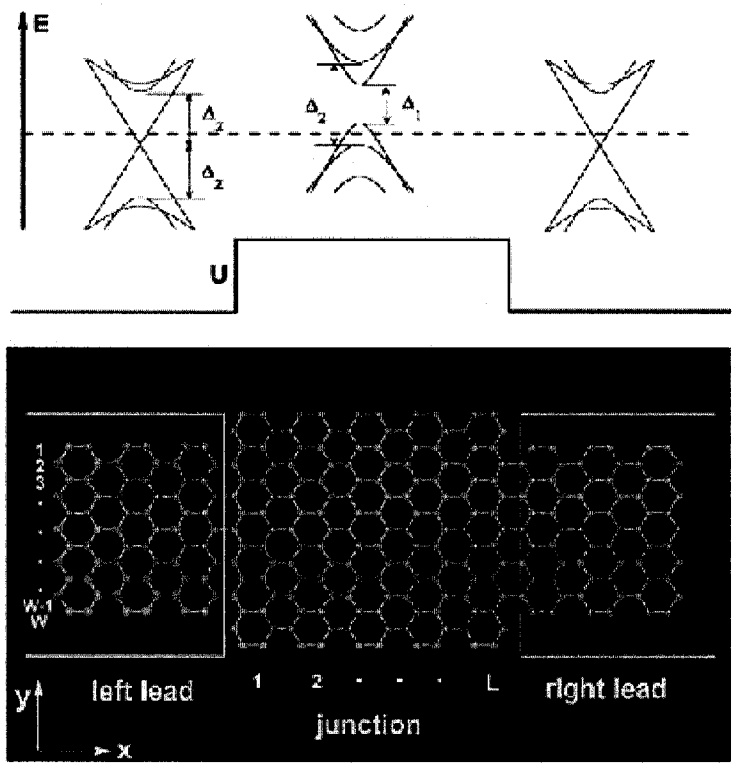

Fig. 4.1: *Schematic diagrams of the energy band dispersions and the proposed graphene switch.*

Our setup is shown in Fig. 4.1. The bottom subgraph of Fig. 4.1 shows the atomic structure of the graphene junction including three regions: left lead, middle graphene region, and right lead. Both leads have the same width with $W = 3m - 1$ to ensure that they are metallic. The width of the middle region is chosen to be $W + 4$ so that it is semiconducting [24]. The top subgraph in Fig. 4.1 shows the dispersion relation of the left, middle and the right region of the switch, respectively. The dashed line denotes the energy E of incident electrons. U is the external potential applied to the middle graphene region. Unlike conventional

parabolic semiconductor energy band diagram ($E \propto k^2$), the energy of the lowest conduction subband in the lead is linearly proportional to the vector $\boldsymbol{k}$ [2]. This dispersion relation indicates that carriers in this channel are massless.

To compute the transport properties of the graphene switch, we use the Landauer-Buttiker formula [48] to calculate the conductance the switch circuit. The retarded self-energy $\sum_L^r$ and $\sum_R^r$ for left and right leads can be obtained as follows

$$\sum_L^r = H_{LC}^+ G_L^r H_{LC}$$

$$\sum_R^r = H_{RC}^+ G_R^r H_{RC} . \tag{4.1}$$

Here the Hamiltonians H_{LC} and H_{RC} represent the coupling between the junction and the leads. They are nonzero only for adjacent points on the interface based on the tight-binding approximation. G_L^r and G_R^r are the retarded surface Green's functions of the left and right semi-infinite leads, which can be calculated using the transfer matrix method [49]. The on-site energy is set to $\varepsilon_{2p} = 0eV$ and the hopping parameter is set to $V = -3.0eV$. The retarded Green's functions of the central junction is

$$G_c^r = (E - H_C - \sum_L^r - \sum_R^r)^{-1} \tag{4.2}$$

Once we obtain the self-energy term $\sum_{L,R}^r$, we can easily calculate the $\Gamma_{L,R}$ that describes the coupling between the junction and the leads.

$$\Gamma_{L,R} = i\left[\sum\nolimits_{L,R}^{r} - \sum\nolimits_{L,R}^{a}\right] \tag{4.3}$$

The advanced self-energy term $\sum_{L,R}^{a}$ in Eq. (4.3) is the Hermitian conjugate of $\sum_{L,R}^{r}$. The transmission function of the graphene switch can be expressed as

$$T = Tr\left[\Gamma_L G_C^r \Gamma_R G_C^a\right]. \tag{4.4}$$

The conductance is proportional to the probability of electron transmission through the junction region, $G = \frac{2e^2}{h}T$. In order to ensure the incident electron energy lies within the single-mode region of the leads and also in the gap of the middle graphene region, we chose $E < \min\left(\frac{\Delta_1}{2}, \Delta_z\right)$. As shown in Fig. 4.1, Δ_1 is the band gap between the lowest conduction subband and the upmost valence subband of the junction, Δ_z is the energy spacing between the bottom of conduction subbands and the next subband within the lead. In the following simulations, we set W=23 and thus obtain the corresponding $\Delta_z = 0.65eV$, $\Delta_1 = 0.38eV$ and $\Delta_2 = 0.79eV$ by the nearest neighbor tight-binding band structure calculation [50].

4.2 Numerical Results

The calculated conductance is shown in Fig. 4.2. By applying an external gate

voltage at the middle graphene region, a potential barrier U appears. In general, if the chosen voltage potential makes the energy of incident electron touch the top of the first valence subband of the junction, the incident electron can easily pass through the junction as expected and the switch should be turned 'on'. However, our simulation results show that the incident electrons are almost completely reflected and the conductance remains almost zero. This phenomenon implies that the carrier has to satisfy an additional condition to pass through the potential barrier.

When the potential barrier U increases further, the switch turns 'on' and the first resonant transmission peak appears around U=0.51 eV for L=20. This behavior can be easily understood by the Klein paradox. That is, with the availability of channels used to transport holes, electrons can transfer through the large potential barrier via these channels without exponential decay. The electron-hole symmetry ensures the successful penetrating of electrons through the high-height barrier. The conductance oscillates above the envelope line and it increases as U increases due to the resonance and anti-resonance transports as shown in Fig. 4.2. Although more channels can allow electrons to pass through and more resonance matching conditions (refer to our later discussion) can be satisfied as U increases, T never exceeds 1. The reason is that the energy of the incident electron is limited within the single-mode region in our calculations. As the length of the junction increases, the first resonant peak becomes sharper and shifts towards left slightly and more resonant peaks appear. These observations can be easily understood by the conventional resonance condition. However, to produce the

first conductance peak, the condition $U > \Delta_2/2 + E = 0.44eV$ is still required. This result strongly suggests that this peak results from the second valence subband.

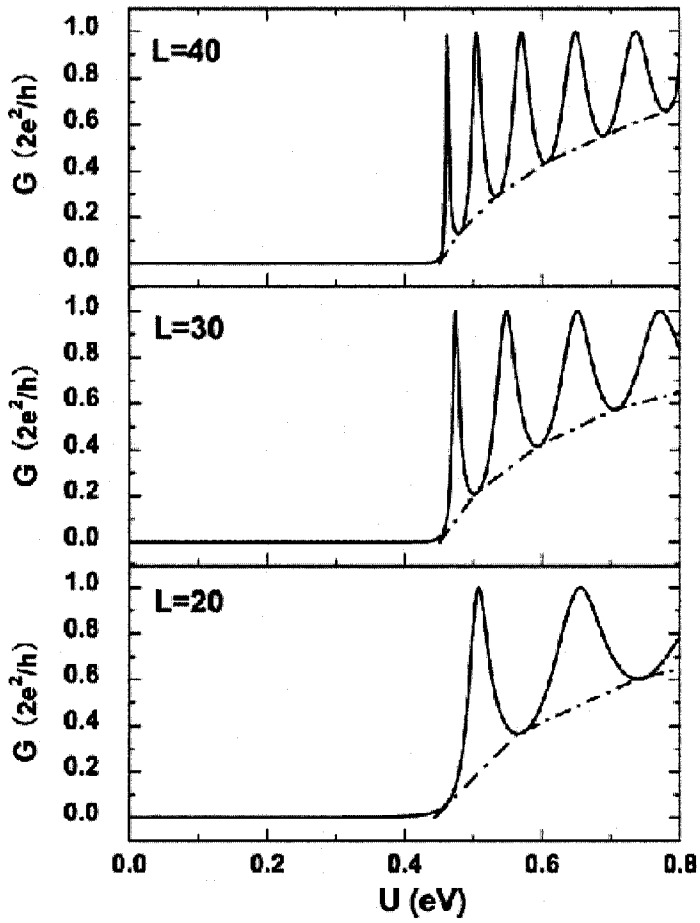

Fig. 4.2: *Conductance vs. the potential height in the single-mode region with different length of the junction. Here W = 23 and E = 0.05eV. The conductance oscillates above the envelope line plotted with dash dot line.*

To verify the above conjecture, Fig. 4.3 shows the conductance as a function of the junction length L calculated by fixing E=0.05 eV and U=0.5 eV. Such a choice provides two conducting channels in the middle region for electrons passing through the junction. In general, the conductance curve should be complicated with some glitches due to the quantum interference between two channels [51]. Surprisingly, our numerical result exhibits a regular periodicity as a function of L in Fig. 4.3. Based on the detailed analysis of this conductance period with the conventional resonance condition, we find that only the second valence subband provides a channel to allow incident electrons to pass, and the first valence subband does not contribute. We also performed similar simulations with different widths (W=17 and 20) and the same phenomenon was observed. This switch behavior actually does not depend on the junction width.

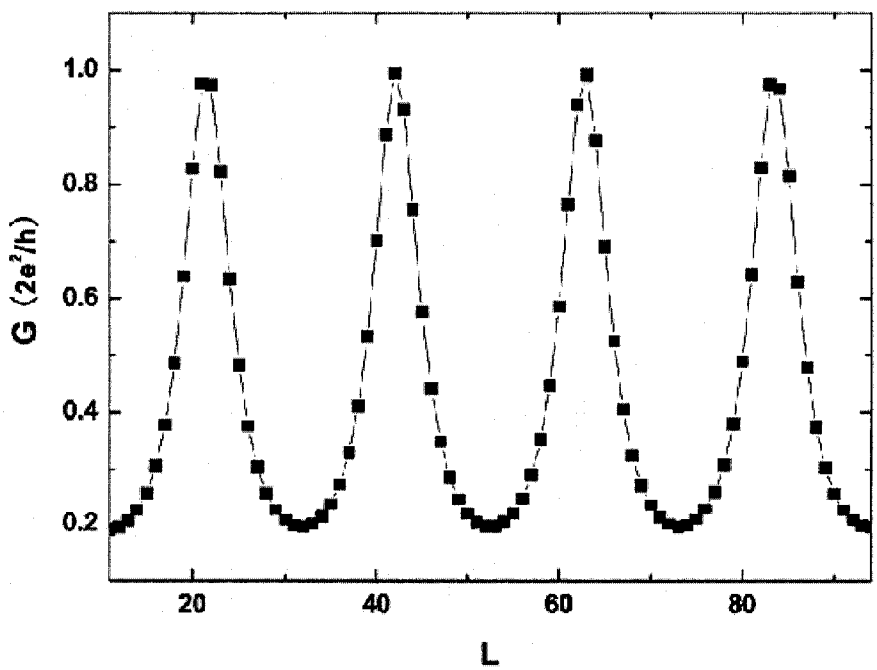

Fig. 4.3: *Conductance versus the length of the junction with W = 23, E = 0.05eV and U = 0.5 eV.*

Generally speaking, to pass through the middle region, electrons have to satisfy conventional resonance condition which usually describes the transfer of an electron through a junction via resonant tunneling (T=1) due to the phase accumulation. It works well in conventional semiconductors when the Schrodinger equation is used. In our switch model, the valence subbands in the middle region can be shifted upwards with the applied external gate voltage to provide conducting channels. When electrons satisfy the conventional resonance condition, $q_x L = N\pi$ with $N = 0, \pm 1, \pm 2, \cdots$, where q_x denotes the x-direction (along the propagation direction) component of wave-vector inside the middle region, they can pass through the junction resonantly. However, our simulation results show that the electron is still prohibited to pass trough the middle region when the conventional resonance condition is satisfied. To understand this anomalous transport behavior more clearly, we derive an analytical expression of the eigenfunction and eigenvalue of the perfect armchair graphene nanoribbon with a finite width (W) as

$$\psi_n^s(j,q_x)=\frac{\sin\left(q_n\frac{\sqrt{3}}{2}aj\right)}{\sqrt{(W+1)\frac{\sqrt{3}}{2}a}}\begin{pmatrix}1\\ s\sqrt{\frac{\mu^*}{\mu}}\end{pmatrix}. \qquad (4.5)$$

$$\varepsilon_n^s(q_x)=sV\sqrt{\mu\mu^*}$$

with $\mu = 2e^{iq_x\frac{a}{2}}\cos\left(q_n\frac{\sqrt{3}}{2}a\right)+e^{-iq_xa}$, $q_n=\frac{n\pi}{\frac{\sqrt{3}}{2}a(W+1)}$,

respectively. Here, a is the C-C bond length ($1.42\overset{0}{A}$), V is the nearest hopping parameter (-3.0 eV), n denotes different subband with 1, · · ·, W. j labels the atomic position in the y-direction with 1,· · ·,W. s=+1 (-1) describes the conduction (valence) subbands, respectively. The chirality of the electron in the conduction subband or hole in the valence subband can be determined by the good quantum number q_x and q_n. To determine the lowest conduction subband or the upmost valence subband, the integer number n needs to satisfy the condition, $n=N\,\mathrm{int}\left[\frac{2}{3}(W+1)\right]$. Here the function of *Nint* rounds off the variable to an integer. To verify that electrons in the lowest conduction subband cannot pass through the switch via the upmost valence subband of the middle region, we calculate the corresponding transfer matrix element P_{11}, and we obtain $P_{11}=\left|\langle s,n,q_x|\hat{V}|s',n',q_x'\rangle\right|^2\simeq 4.5\times10^{-14}eV^2$ with W=23, s=+1, n=16, s'=-1, and n'=19. Here, $\hat{V}=V\sum_j|j\rangle\langle j+2|$ with j=2, 4, 6, · · ·, W-1 is the scattering operator

coming from the sharp interface between the lead and the middle region. In the elastic scattering process in our system, the equation $\varepsilon_n^{+1}(q_x) = \varepsilon_{n'}^{-1}(q_x') + U$ has to be satisfied. Meanwhile, the applied voltage U is large enough to ensure the equation has a real numerical solution (q_x'). The transfer matrix element P_{12} between the lowest conduction subband to the second upmost valence subband is calculated to be around 0.27 eV^2. In our switch design, the values in these transfer matrix elements are almost independent of the width of graphene nanoribbon based on our numerical simulations.

The sharp interface in our design plays an important role, which was not observed in its 2-D counterpart [10]. From our numerical results, it is clear that the selective tunneling corresponding to two transfer matrix elements (P_{11} and P_{12}) can illustrate the interesting transport process. When U>0.24 eV, the first valence subband of the middle region is moved high enough to provide a conducting channel, but P_{11} almost equals to zero. That is to say, no matter whether the chirality of electrons are conserved or not, the sharp interface in this symmetrical connection prevents the tunneling process. Electrons, therefore, are bounced back and the conductance remains almost zero, as shown in Fig. 4.2. Increasing the length of the junction only changes the conventional resonance condition, but the conductance still remains zero. When we further increase the voltage potential to U>0.44 eV, the second valence subband of the middle region moves upwards. The energy of incident electrons touches this channel and the electrons can then

tunnel through the potential barrier without exponential decay.

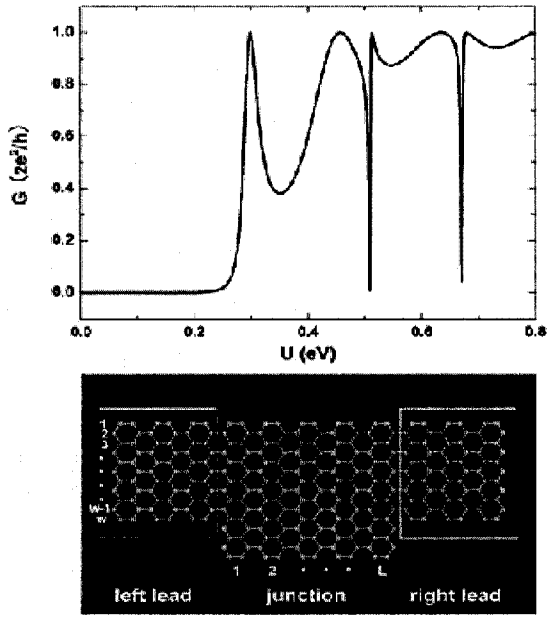

Fig. 4.4: *Top subgraph: conductance vs. the potential height in the single-mode region. Bottom subgraph: atomic structure of the T-shaped junction. Here W = 23, L = 20 and E = 0.05eV.*

Note that whether the first valence subband contributes to the conductance or not depends strongly on the geometric structure of the graphene nanoribbon junction. As an example, a T-shaped junction with the same width of the previous symmetry structure is shown in Fig. 4.4. By choosing the same parameters (E=0.05 eV, W=23 and L=20) as in the case of Fig. 4.3, numerical results in Fig. 4.4 show clearly that the first conductance peak appears in the region where the incident energy touches the first valence subband (0.24eV<U<0.44 eV). The reason is that the transfer matrix element ($P11$) has a finite value (about 0.24 eV^2)

in the T-shaped junction. Our results suggest that the switch conducting behavior can be manipulated by tailoring the graphene nanoribbon. In the range of $0.44\text{eV}<U<0.7\text{eV}$, another interesting observation is that two obvious conductance dips appear in the conductance curve. This phenomenon can be attributed to the destructive interference effect between two conducting channels [52].

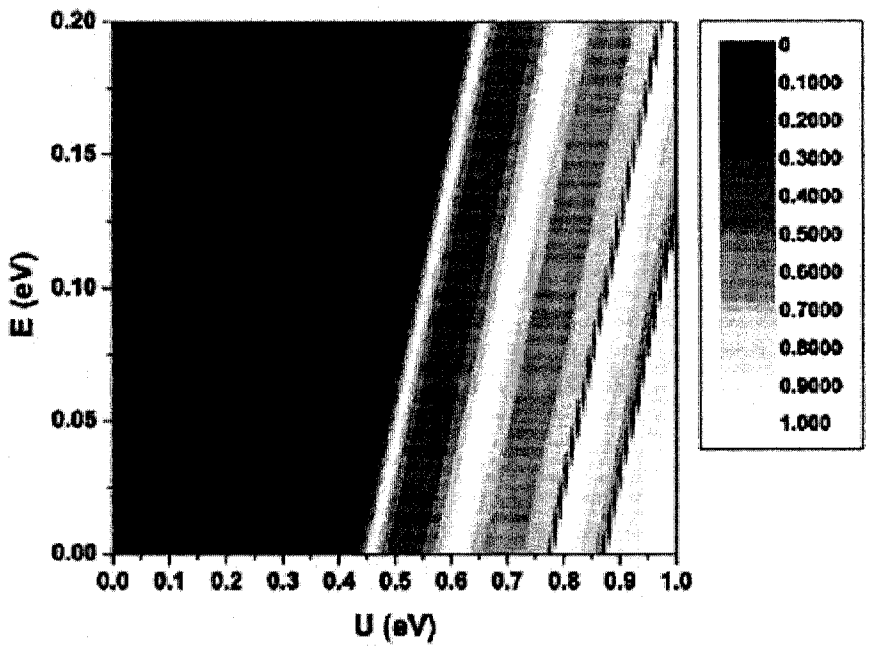

Fig. 4.5: *Three-dimensional plot of conductance as the function of energy and potential height for the configuration shown in Fig. 4.1. Here W=23 and L=20.*

To illustrate the switch effect more clearly in the single-mode region, Fig. 4.5 presents a three-dimensional color picture to display the conductance as a

function of incident electron energy (E) and the potential barrier height (U) for the configuration shown in Fig. 4.1. The color is scaled with the corresponding conductance, white and blue colors correspond to T=1 ('on') and T=0 ('off'), respectively. It is clear that the figure can be roughly divided into two regions bounded by the first peak (the most left white line). At the left of the first peak (the first white line), the switch stays off or all incident electrons are bounced back. The junction begins to be turned 'on' starting from the right of the first peak by applying a certain threshold bias U and its conductance oscillates with increasing U as shown in Fig. 4.2. Although more channels can allow electrons pass through or more resonance matching conditions can be satisfied as U increases, T never exceeds 1. The reason is that the energy of incident electrons is limited within the single-mode region in our calculations. Several additional interesting features can be observed in Fig. 4.5: **(i)** The peaks or the white lines are parallel to each other and shift toward the right as the incident energy increases. **(ii)** All peaks are straight lines indicating the required voltage to open the switch increases linearly as incident electron energy increases. **(iii)** The white lines become wider and blue lines become narrower as U increases. The confinement of electrons is a basic requirement to realize a qubit in a solid device. In addition to the switch design, the selective tunneling rule observed in the symmetrical nanoribbon suggests that we can achieve the confinement of an electron in the middle region even though the region connects to two metallic leads. The condition for such a confinement is $\Delta_z > |\Delta_1 + U|$. The external bias

voltage U can be adjusted to control whether the trapped electrons to pass through the middle region or not. Our design is easier to implement than that in Ref. [52]. Compared to that in a GaAs quantum dot, our qubit design in graphene nanoribbon is very promising because the spin-orbit interaction and hyperfine interaction in graphene are considerably weak [53]. The time of spin decoherence is longer and one can exploit the electron-spin freedom to design quantum qubit. As a result, the qubit in the graphene nanoribbon can possibly operate at room temperature.

4.3 Discussion

In this chapter, the transport properties of a semiconducting graphene nanoribbon sandwiched between two metallic graphene nanoribbon leads are investigated. Switching behavior is observed according to our numerical results. The junction has a good "on-off" ratio performance, which is almost completely pinched-off without external gate voltage and can be turned 'on' by applying a threshold bias voltage. We find that our numerical results are related closely to the Klein phenomenon. Electrons can pass through the junction when these Dirac Fermions satisfy both the conventional resonance condition and the selective tunneling rule. These findings are helpful for us to construct and design graphene nanoelectronic devices in the near future. For instance, the proposed graphene switch can be used to achieve qubit design in quantum computers.

Chapter 5

Graphene Rectifiers and Transistors

In this chapter, we present our model for graphene rectifier and transistor design. Zhengfei Wang and I did this research at University of Alberta in March 2007 under th supervision of Dr. Jie Chen and Dr. Qinwei Shi and the paper is under review (after 2nd-round modification). In Section 5.1, the quantum conductivity of a Z-shaped GNR is calculated based on the Landauer-Buttiker formula and the TB model. We find that an external gate voltage applied in the junction region is sufficient to rectify electrons across the junction. Rectification is also found independent of the width and length of the junction, which is the intrinsic property of Z-junction. In Section 5.2, we demonstrate that the Z-shaped GNR can be further extended to design a field-effect transistor (FET). By applying a local gate bias in the center of the armchair ribbon, the device current-voltage (I-V) characteristics clearly show asymmetric with respect to the bias polarity and exhibit that it can work as an n-type or p-type transistors by changing the polarity of gate bias without doping.

5.1 Z-junction Graphene Rectifier

To study the transport proprieties of the Z-junction GNR, we separate the device as shown in Fig. 5.1 into three regions: the left lead, the middle junction, and the right lead. In this study, we assume that the junction width is W-1 while both the left and right leads have equal width W (W is an integer number). The length of the junction is L where L is an integer number. In our design, the leads are semi-infinite armchair GNR, but the junction is zigzag GNR.

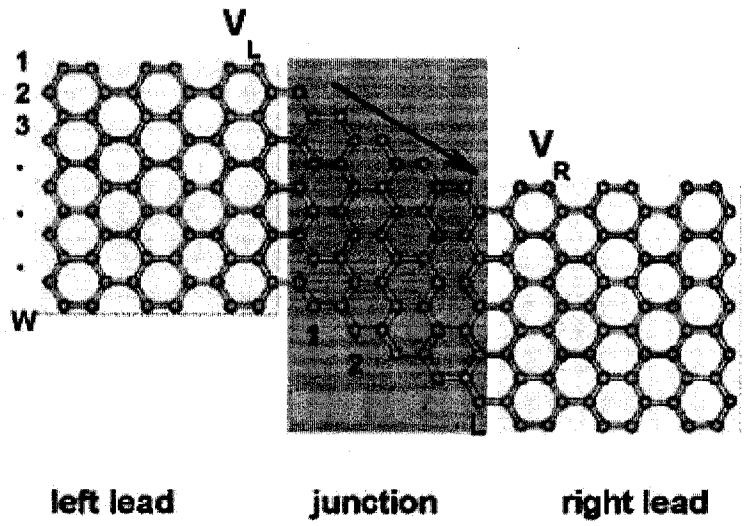

Fig. 5.1: *Schematic graph of a rectification circuit made of Z-junction GNR. The width of the left/right lead and the junction are integer W and W -1, respectively. The length of the junction is integer L.* $V_{L/R}$ *is applied voltage on left/right lead. Current is positive if electrons flow towards the junction and otherwise negative.*

We use the Landauer-Buttiker formula to solve the transmission coefficients of

this device. The scheme was introduced in Chapter 4. By using the Landauer-Buttiker formalua, current I passing through the junction as the function of applied voltages $V_{L/R}$ can be expressed as

$$I = \frac{2e}{h}\int_{-\infty}^{+\infty} dE\left[f(\mu_L) - f(\mu_R)\right]T(E), \tag{5.1}$$

where f is the Fermi function. It is expressed in terms of temperature T and Boltzmann's constant k_b, which is $f(\mu_{L/R}) = 1/\left[1+\exp(E-\mu_{L/R})/k_bT\right]$. $\mu_{L/R} = E_f - eV_{L/R}$ and E_f is the Fermi energy. In the following calculation, we set $E_f = 0$.

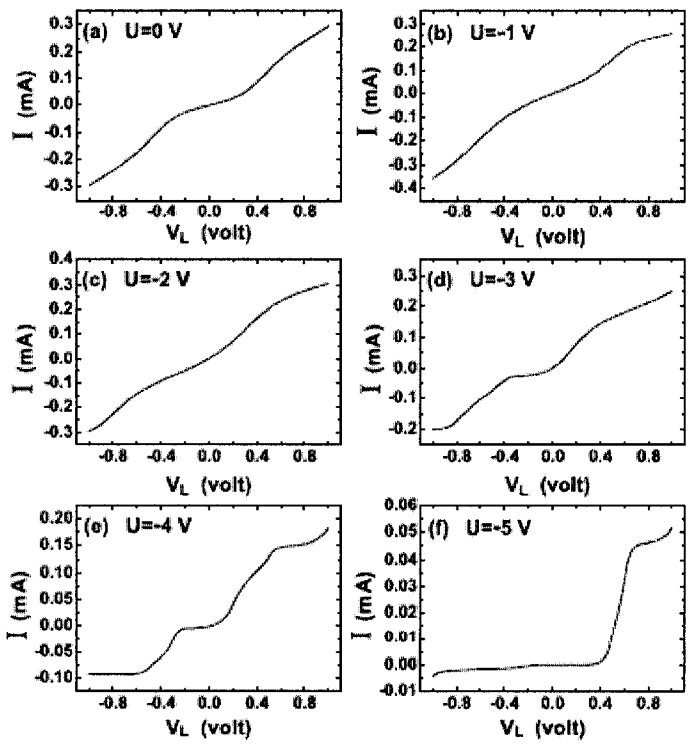

Fig. 5.2: *The calculated I-V curves for the Z-junction GNR with different gate*

voltage from (a)-(f). In our simulations, we choose $W = 5$, $L = 6$, $V_R = 0V$, $E_f = 0eV$ *and* $T = 300K$.

The numerical results of I-V curves are shown in Fig.5.2 (a)-(f). There are two distinct characters that we can see from these figures. (i) Without the gate voltage ($U = 0V$), the I-V curve is symmetry with respect to the positive and negative bias voltage (V_L), shown in Fig. 5.2(a). (ii) By applying a gate voltage in the central junction region, the curves become more asymmetry, as shown from Fig. 5.2 (b) to (f). In Fig. 5.2 (f), the current is almost quenched to zero between $-1.0V \sim 0.4V$. The current begins to increase only when the positive bias voltage larger than a thresh-old value ($\simeq 0.4V$). This behavior shows the typical rectification proprieties. Therefore, when the applied gate voltage large to -5V, in this Z shaped junction structure can achieve a perfect rectified function in the bias voltage range between $-1V \sim 1V$. Similar behaviors can also be observed with a positive gate voltage. For $U = 5V$, the current is quenched in the range between $-0.4V \sim 1V$, and it begins to increase towards the opposite direction when the negative bias voltage large than $-0.4V$.

In order to explain the phenomenon that why the Z-shaped junction with an external gate voltage can realize rectified effect, we further calculate the eigenstates of this open system. Its Hamilton can be expressed as

$$H = H_C + \sum\nolimits_L^r + \sum\nolimits_R^r \quad . \tag{5.2}$$

Here, the contribution of the left and right leads is included in the self-energy term. The corresponding density of states (DOS) of this open system [50] is

$$DOS(E) = \sum_{\alpha} \frac{1}{2\pi} \frac{\gamma_{\alpha}}{\left(E - \varepsilon_{\alpha}\right)^2 + \left(\gamma_{\alpha}\right)^2} . \tag{5.3}$$

The summation is done over all eigenvalues. ε_{α} is the real part of eigenvalue and represents the position of the resonance state. γ_{α} is the image part of the eigenvalue and represents the broad of the resonance state.

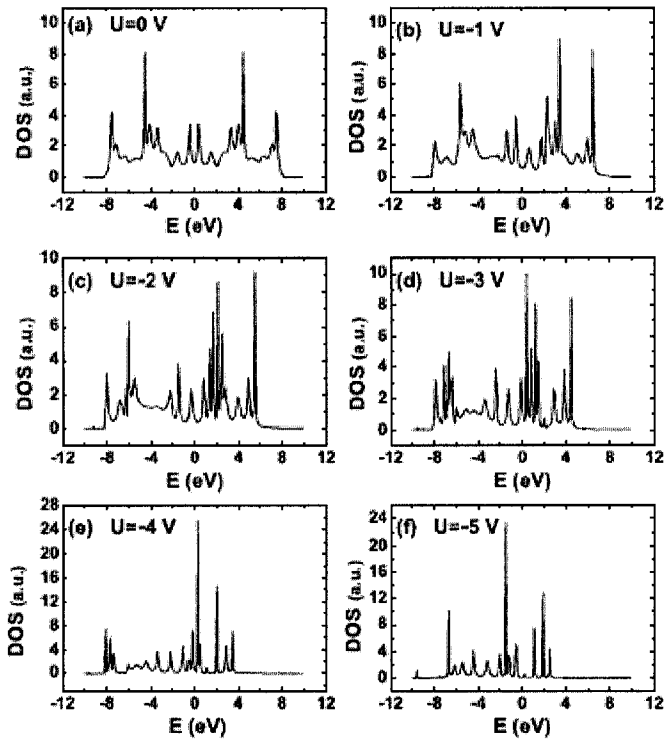

Fig. 5.3: *The calculated DOS for the junction part of the device with different external gate voltage (we can compare them with Fig. 5.2(a)-(f)). Here, W = 5, L = 6.*

Fig. 5.3 shows the DOS of the system by using the same parameters as those in Fig. 5.2. For U = 0V, the DOS is symmetry with respect to the positive and negative energy. In contrast, by increasing the external gate voltage from U = -1V to -5V, the DOS gradually localizes in the negative energy region as shown in Fig. 5.3(b)-(f). Noticing the fact that the main contribution to the current in the integral expression of Eq. (5.1) is between the energy range of the chemical potential of left lead ($\mu_L = -eV_L$) and right lead ($\mu_R = 0$). That is to say, for the positive bias voltage, tunneling channels in negative energy region contribute to the current. While for the negative bias voltage, tunneling channels in positive energy region contribute to the current. The localization of DOS in the negative energy range, therefore, provides more tunneling channels in negative energy than in positive energy range, which directly results in the asymmetry of the I-V curve in Fig. 5.2. This conclusion is consistent with the previous studies for the nanotube Y junction rectified circuit [54, 55].

From our previous discussion, we propose a simple model to show the rectified effect for a Z-shaped junction, and we also explain the causes of this phenomenon. However, there is still one question that we have not answered yet: "whether this rectified effect universally exists in our model?", or "is it just a special case for a particular structure?". In order to answer this question, we further calculate the I-V curve of the rectifier using different junction width and length in the following section. The corresponding results are shown in Fig. 5.4. Firstly, for a junction

with the length of $L = 20$, we change its width with $W = 23, 29, 35$ as shown in Fig. 5. 4 (a), (b) and (c). The common characters of the I-V curves are that there always exists a certain range where the current is quenched to zero. When the positive bias voltage gets large than a threshold value, the current starts to increase. For $W = 23$ and 35, the quenched region is wider than that for $W = 29$. Secondly, we fix the width ($W = 17$) of the junction, and change the length of the junction with $L = 20, 40,$ and 60 as shown in Fig. 5.4(d), (e) and (f). Similar rectified behaviors can be observed. In addition, the quenched region almost does not change with the increasing length of the junction, which behaves different from that of changing the width of the junction. From our numerical results, we can conclude that our rectified circuit model is general and does not depend on the detailed structure of the junction. This finding can significantly reduce experimental difficulties and provides more convenience to validate our model in real experiment.

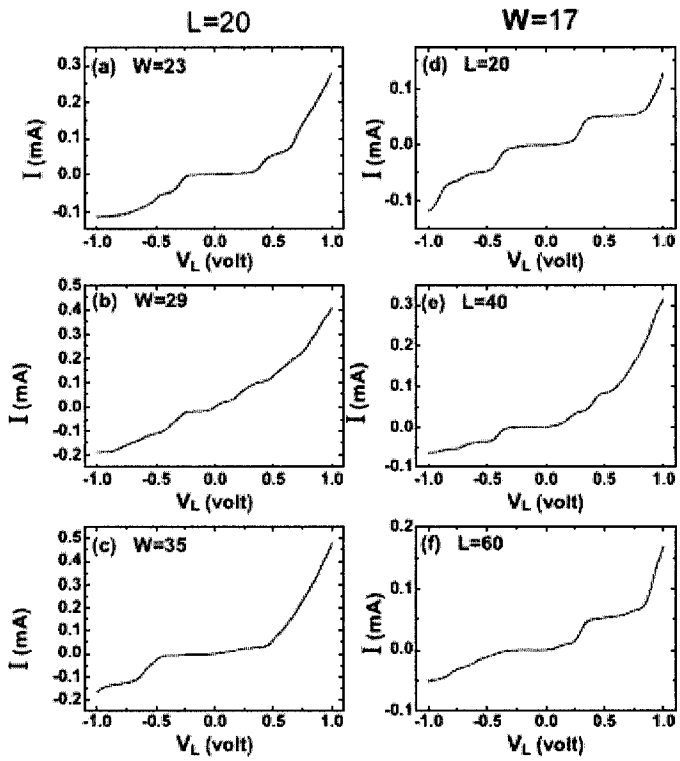

Fig. 5.4: *The calculated I-V curves for the Z-junction GNR as shown in Fig. 5.1 with different lengths and widths. Here, we choose* $V_R = 0V$, $E_f = 0eV$ *and* $U = -5V$.

5.2 Graphene Transistor

In this section, we propose a p-type or n-type GNR transistor by applying a negative or positive gate voltage in the center conductance region of GNR. The schematic graph is shown in Fig. 5.5.

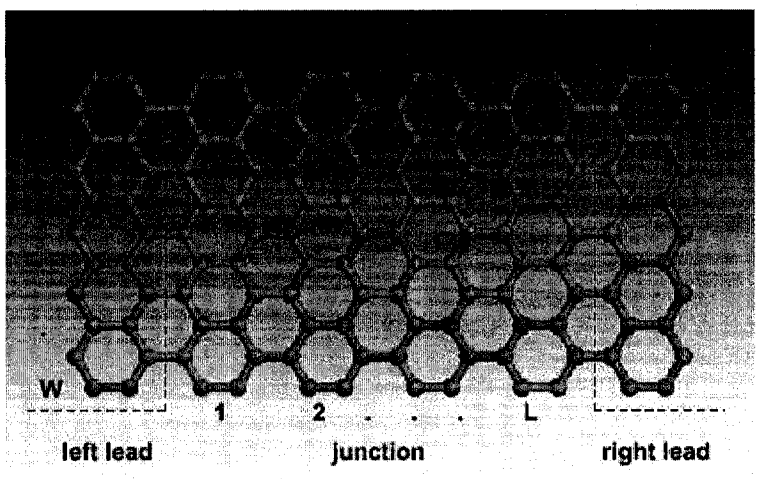

Fig. 5.5: *Schematic graph of armchair graphene ribbon transistor. The width of the left/right lead and the junction are integer W. The length of the junction is integer L. VL=R is applied voltage on left/right lead. Current is positive if electrons flow towards the junction and otherwise it is negative.*

The typical I-V curves of the transistor are shown in Fig.5.6. There are two distinct characteristics that we can see from Fig. 5.6 (a). (i) Similar to the Z-shaped junction rectified device, without the gate voltage ($Vg = 0V$), the I-V curve is symmetry with respect to the bias voltage (V_L). The curves, however, become more asymmetric when the gate voltage increases in the central junction region. When the gate voltage increases to $6V$, the current is quenched to zero in the positive bias voltage region, which shows a typical rectification effect. (ii) In the positive bias voltage region, the current drops with increasing gate voltage. This I-V behaves the same as an n-type doped transistor. In Fig.5.6 (b), the curve is the mirror image of Fig. 5.6 (a) but rotates by 180^0 around the origin of the coordinate.

In this case, a p-type transistor can be achieved when the applied gate voltage becomes negative.

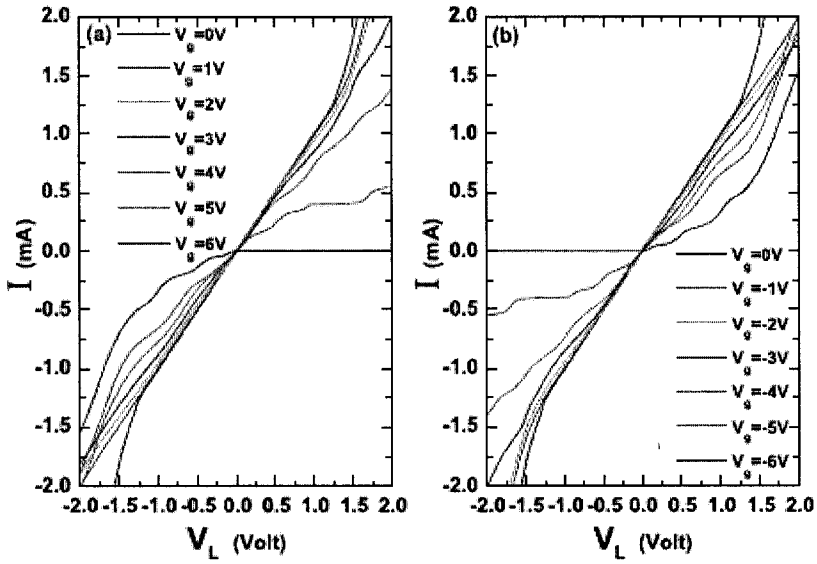

Fig. 5.6: *The calculated I-V curves for the armchair GNR with different gate voltage Vg. (a) positive gate voltage. (b) negative gate voltage. In our calculation, we choose W = 11, L = 4, V_R = 0V , E_f= 0eV and T = 300K.*

The above results show that we can simply realize the n-type or the p-type transistor by changing the applied gate voltage on the armchair graphene ribbon, which is much simplier than that using doping.

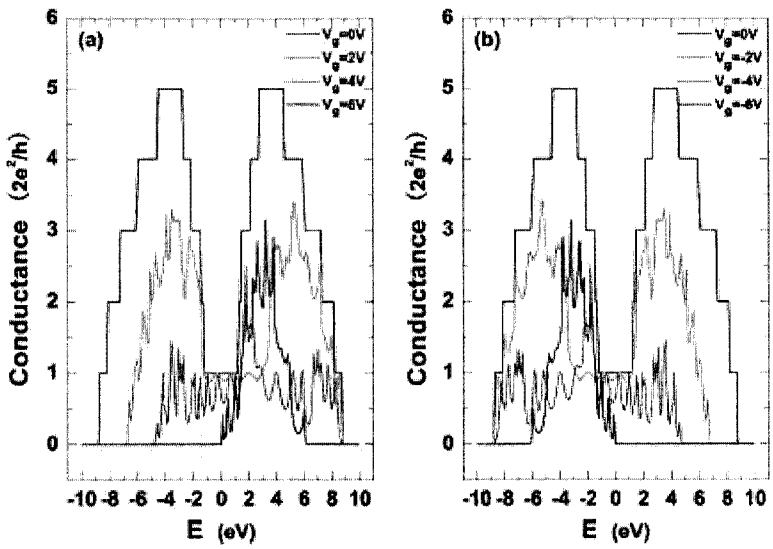

Fig. 5.7: *The calculated conductance for armchair graphene nanoribbon with different gate voltage Vg. Here, W = 11* and *L = 4.*

A commonly asked question is: "Why the applied gate voltage can turn the electron in armchair graphene nanoribbon to realize this transistor effect?" To explain this phenomenon clearly, we also plot the conductance of the ribbon as shown in Fig. 5.7 (a) and 5.7 (b). In Fig.5.7 (a), without the gate voltage, the conductance shows the typical step curve (here we choose the width of the ribbon $W = 11$ so that it is metallic). When we increase the gate voltage, the conductance is suppressed down and no clear step can be observed anymore. In addition, these curves become more asymmetric with respect to the bias voltage. When the gate voltage gets larger than $6V$, the conductance is almost localized in the positive energy section. Similar to our previous discussion of the density of state (DOS) in the rectified device, tunneling channels in negative energy region contribute to

current when a positive bias voltage is applied. Likewise, tunneling channels in positive energy region contribute to the current when a negative bias voltage is applied. This behavior can explain the asymmetry of the I-V curves. The drop of the current curve can cause the decreasing of the intensity of the conductance curves in Fig. 5.6 (b) and 5.7 (b), which can be explained in the similar way.

5.3 Discussion

By using graphene nanoribbons, we have designed two nanoscale devices. The external gate voltage applied in the junction region can control the device behavior and achieve the design of a GNR switch, a GNR rectifier and even a GNR transistor. Overall, our model provides a new insight to design functional nanoscale electronic device based on GNRs.

Chapter 6

Conclusion

We investigate the fundamental physical and electrical properties of graphene ribbons (GNRs). We also explore GNRs to make nanoelectronic devices. Specifically, we use both the analytical tight-binding method and the numerical first-principles calculations to study the electronic structures of GNRs. We discovered that perfect armchair GNRs are metallic (zero energy gap) materials when the width n=3p+2, where p is an integer; otherwise, insulating (non-zero energy gap). However, the existence of dangling bonds at the edges of GNRs provides a great opportunity to tune their properties by attaching different kinds of chemical molecules to the edges. With both analytical and numerical methods, we demonstrated that the chemical modifications can affect the geometric and electronic structures dramatically and even lead to metal-to-insulator transition. For instance, we found that armchair GNRs with dangling bonds saturated by hydrogen atoms are all insulators with non-zero energy gaps. These findings can help us gain insights about electronic transport in GNRs. Furthermore, based on the understanding of electronic properties of GNRs, we propose some designs of GNR-based devices. The proposed nanodevice designs not only well illustrate the physics behind these phenomena, but also provide a guideline towards the experimental realizations of such novel devices and their integrated nanocircuits.

Bibliography

[1] Richard Van Noorden, Nature **442**, 228 (2006).

[2] K. S. Novoselov, A. K. Geim, S. V. Morozov, D. Jiang, M. I. Katsnelson, I. V. Grigorieva, S. V. Dubonos, and A. A. Firsov, Nature **438**, 197 (2005).

[3] K. S. Novoselov, A. K. Geim, S. V. Morozov, D. Jiang, Y. Zhang, S. V. Dubonos, I. V. Grigorieva, and A. A. Firsov, Science **306**, 666 (2004).

[4] A. Krishnan *et al.*, Nature **388**, 451 (1997).

[5] H. Shioyama, J. Mat. Sci. Lett. **20**, 499 (2001).

[6] Sasha Stankovich, Dmitriy A. Dikin1, *et al.*, Nature **442**, 282 (2006).

[7] Taisuke Ohta, Aaron Bostwick, Thomas Seyller, Karsten Horn and Eli Rotenberg, Science **313**, 951 (2006).

[8] A. Hashimoto, K. Suenaga, A. Gloter, K. Urita, S. Iijima , Nature **430**, 870 (2004).

[9] Yuanbo Zhang, Yan-Wen Tan, Horst L. Stormer and Philip Kim, Nature **438**, 201 (2005).

[10] M. I. Katsnelson, K. S. Novoselov, A. K. Geim, Nature Physics **2**, 620 (2006).

[11] C. Berger, Z. Song, X. Li, X. Wu, N. Brown, C. Naud, D. Mayou, T. Li, J. Hass, A. N. Marchenkov, E. H. Conrad, P. N. First and W. A. de Heer, Science **312**, 1191 (2006).

[12] "Graphene Calling", Nature Materials **6**, 169 (2007).

[13] http://www.nature.com/conferences/aps

[14] Geim, A. K. & Novoselov, K. S. Nature Mater. **6**, 183 (2006).

[15] Landau, L. D. & Lifshitz, E. M. *Statistical Physics, Part I* (Pergamon, Oxford, 1980).

[16] Venables, J. A., Spiller, G. D. T. & Hanbucken, M. Nucleation and growth of thin films. *Rep. Prog. Phys.* **47**, 399–459 (1984).

[17] Evans, J. W., Thiel, P. A. & Bartelt, M. C. Morphological evolution during epitaxial thin film growth: Formation of 2D islands and 3D mounds. *Sur. Sci. Rep.* **61**, 1–128 (2006).

[18] Klein, O. Die reflexion von elektronen an einem potentialsprung nach der relativistichen dynamic von Dirac. Z. Phys. 53, 157 (1929).

[19] Greiner, W., Mueller, B. & Mostepaneenko, V. M. Vacuum Effects in Strong Fields (Springer, Berlin, 1985).

[20] Schedin, F. et al. Detection of individual gas molecules by graphene sensors. Preprint at http://arxiv.org/abs/cond-mat/0610809 (2006).

[21] M.C. Lemme, T.J. Echtermeyer, M. Baus, and H. Kurz, IEEE Trans. Electron Dev., Vol. **28**, No. 4, April 2007.

[22] V. V. Cheianov, V. Falko, B. L. Altshuler, Science **315**, 1252 (2007).

[23] J. B. Pendry, Phys. Rev. Lett. **85**, 3966 (2000).

[24] K. Nakada and M. Fujita, Phys. Rev. B **54**, 17954 (1996).

[25] K. Sasaki, S. Murakami, and R. Saito, J. Phys. Soc. Jpn. **75**, 74713 (2006).

[26] K. Sasaki, S. Murakami, and R. Saito, Appl. Phys. Lett. **88**, 113110 (2006).

[27] L. Brey and H. A. Fertig, Phys. Rev. B **73**, 235411 (2006).

[28] K. Wakabayashi, M. Fujita, H. Ajiki, and M. Sigrist, Phys. Rev. B **59**, 8271 (1999).

[29] H. Ajiki and T. Ando, J. Phys. Soc. Jpn. **62**, 1255 (1992).

[30] Y.-W. Son, M. L. Cohen, and S. G. Louie, Phys. Rev. Lett. **97**, 216803 (2006).

[31] M. Ezawa, Phys. Rev. B **73**, 045432 (2006).

[32] T. Kawai, Y. Miyamoto, O. Sugino, and Y. Koga, Phys. Rev. B **62**, R16349 (2000).

[33] Y.-W. Son, M. L. Cohen, and S. G. Lioue, Nature (London) **444**, 347 (2006).

[34] D. Porezag, T. Frauenheim, T. Kohler, G. Seifert, and R. Kaschner, Phys. Rev. B **51**, 12947 (1995).

[35] Huaixiu Zheng, Z. F. Wang, Tao Luo, Q. W. Shi, and Jie Chen, Phys. Rev. B **75**, 165414 (2007).

[36] K. Sasaki, S. S. Murakami, and R. Saito J. Phys. Soc. Jpn. **75**, 074713 (2006).

[37] M. Burghard, Surf. Sci. Rep. **58**, 1 (2005).

[38] X. Lu and Z. F. Chen, Chem. Rev. (Washington, D.C.) **105**, 3643 (2005).

[39] J. Taylor, M. Brandyge, and K. Stokbro, Phys. Rev. B **68**, 121101 (2003); M. Ernzerhof, M. Zhuang, and P. Rocheleau, J. Chem. Phys. **123**, 134704 (2005).

[40] M. Fujita, K. Wakabayashi, K. Nakada, and K. Kusakabe, J. Phys. Soc. Jpn. **65**, 1920 (1996).

[41] G. Kresse and J. Hafner, Phys. Rev. B **49**, 14251 (1994).

[42] G. Kresse and J. Furthmüller, Comput. Mater. Sci. **6**, 15 (1996); Phys. Rev. B **54**, 11169 (1996).

[43] D. M. Ceperley and B. J. Alder, Phys. Rev. Lett. **45**, 566 (1980); J. P. Perdew and A. Zunger, Phys. Rev. B **23**, 5048 (1981).

[44] P. Hohenberg and W. Kohn, Phys. Rev. **136**, B864 (1964); W. Kohn and L. J. Sham, Phys. Rev. **140**, A1133 (1965).

[45] D. Vanderbilt, Phys. Rev. B **41**, 7892 (1990).

[46] J. M. Soler, E. Artacho, J. D. Gale, A. García, J. Junquera, P. Ordejón, and D. Sánchez-Portal, J. Phys.: Condens. Matter **14**, 2745 (2002).

[47] D. Porezag, Th. Frauenheim, Th. Kohler, G. Seifert, and R. Kaschner, Phys. Rev. B **51**, 12947 (1995).

[48] R. Landauer, Philos. Mag. **21**, 863 (1970).

[49] J. Zhang, Q. W. Shi, and J. Yang, J. Chem. Phys. **120**, 7733 (2004).

[50] Datta, S. *Electronic Transport in Mesoscopic Systems*; Cambridge University Press, New York (1995).

[51] C. P. Chang, Y. C. Huang, C. L. Lu, J. H. Ho, T. S. Li, and M. F. Lin, Carbon **44**, 508 (2006).

[52] K. Wakabayashi, and M. Sigrist, Phys. Rev. Lett. **84**, 3390 (2000).

[53] (a) Trauzette, B.; Bulaev, D. V.; Loss, D.; Burkard, G. cond-mat/0611252; (b) Nilsson, J.; Castro Neto, A. H.; Guinea, F.; Peres, N. M. R. cond-mat/0607343.

[54] A. N. Andriotis, M. Menon, D. Srivastava, and L. Chernozatonskii, Phys. Rev. B **65**, 165416 (2002).

[55] A. N. Andriotis, M. Menon, D. Srivastava, and L. Chernozatonskii, Phys. Rev. Lett. **87**, 066802 (2001).